Chapter 1

Introduction

This chapter presents a comprehensive overview of interferometry using low-coherent light and vortices. It explores the properties of coherent and incoherent light, and their relevance to interferometry. The generation and detection of vortices in coherent light are thoroughly discussed. The work also examines the unique properties of low-coherent light and its relationship with optical coherence. The existing techniques for scalar and vectorial coherence measurement is discussed. Finally, the integration of vortices with low-coherent light is analyzed, highlighting novel phenomena and their implications. Finally, this section concludes with an objective of thesis the motivation driving this research, setting the stage for further innovations in coherence optics and vortex beam applications.

1.1 Light sources

In physics, light is defined as electromagnetic radiation that spans a spectrum of wavelengths, some visible to humans and others not. The portion we can see—visible light—ranges from 400 to 700 nanometers in wavelength and has properties such as frequency, intensity, and propagation speed [1]. Light plays a central role in our perception of the world, enabling us to see colors like green in grass, yellow in sunflowers, and orange in sunsets. A diverse range of sources contributes to the emission of visible light. They can be broadly classified based on their coherence properties into three main categories: coherent, partially coherent and incoherent sources. Coherence, both temporal and spatial, is a crucial factor that affects the interference and imaging capabilities of light, making the choice of light source central to many experimental and practical applications including imaging, information photonics, and holography, etc.

1.1.1 Coherent light sources

Coherent light sources produce light waves that maintain a constant phase relationship over time and space [2]. This coherence allows them to produce interference patterns, which are essential in applications like holography, interferometry, and advanced imaging techniques. Lasers (Light Amplification by Stimulated Emission of Radiation) are the most widely used coherent light sources due to their high degree of spatial and temporal coherence.

- **Properties of Lasers**:
    - **Monochromaticity**: Lasers emit light at a specific wavelength, producing a quasi-monochromatic light.
    - **High Directionality**: Laser beams have a high degree of directionality, allowing them to travel long distances with minimal spread.

  - **Temporal and Spatial Coherence**: Lasers exhibit both temporal and spatial coherence, enabling precise interference-based applications.
  - **High Intensity**: Laser sources can achieve high intensities, which are beneficial for cutting, medical applications, and nonlinear optics.

- **Types of Lasers**:
  - **Gas Lasers** (e.g., Helium-Neon lasers): Known for stable coherence properties, used in holography and precision measurement.
  - **Solid-State Lasers** (e.g., Nd lasers): High-power sources widely used in industrial and medical applications.
  - **Diode Lasers**: Compact and efficient, commonly used in communication and consumer electronics.

Due to these properties, lasers have become indispensable in optical experiments requiring high coherence and precision.

1.1.2 Incoherent light sources

Incoherent light sources, known for their broad spectral emission and low coherence, offer distinct advantages across various applications [2]. Their wide wavelength range produces diffuse, soft lighting that's ideal for general illumination and imaging where precision coherence isn't necessary. Additionally, these sources are often energy-efficient, versatile, and widely available. Examples include light-emitting diodes (LEDs), incandescent bulbs, fluorescent lamps, etc.

- **Properties of LEDs**:

- **Moderate Spectral Width**: LEDs emit light over a broad wavelength range, which can be tuned to produce various colors.
- **Low Spatial Coherence**: LEDs have low spatial coherence, making them ideal for diffuse lighting applications.
- **Efficient and Low Power Consumption**: LEDs are energy-efficient, with minimal heat generation compared to traditional incandescent bulbs.
- **Longevity and Durability**: LEDs have longer operational lifetimes, which makes them practical for industrial and consumer lighting.

- **Properties of Incandescent Bulbs**:
  - **Broad Spectral Emission**: Incandescent bulbs emit light across a wide range of wavelengths, appearing as white light.
  - **Low Efficiency**: A significant portion of the energy in incandescent bulbs is dissipated as heat rather than light.
  - **Very Low Coherence**: Incandescent sources are entirely incoherent, which prevents their use in applications requiring high coherence.

1.2 Interferometry with coherent light beams

Optical interferometers are devices designed to create and analyze interference patterns between multiple light beams, providing insights based on either the light's travel path or the properties of the light source. The simplest interference setup involves splitting light from a source into two beams that travel distinct paths and then overlap on a detection surface. The combined intensity at the observation point differs from the sum of each beam's individual intensities, producing alternating bright and dark regions known as interference fringes, which are characteristic of the interference effect [3, 4].

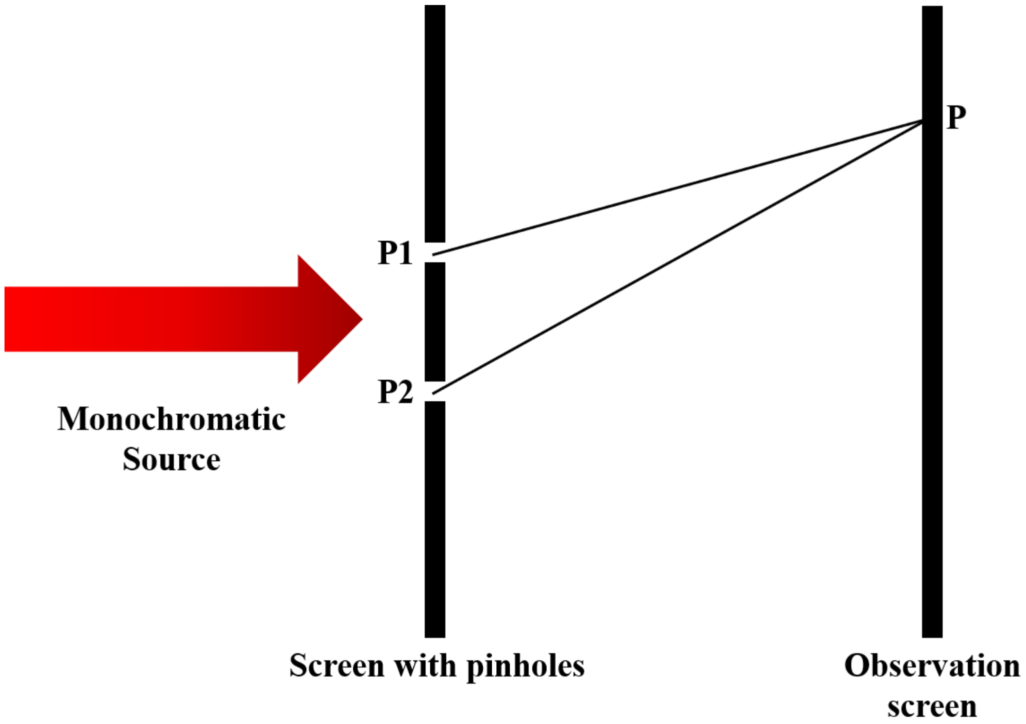

Fig. 1.1 Interference with a monochromatic source.

When two monochromatic waves moving in the same direction and polarized in the same plane converge at a point P as shown in Fig. 1.1, their combined electric field at that point is given by

$$U = U_1 + U_2, \tag{1.1}$$

where U_1 and U_2 represent the electric fields of the individual waves. If these waves share the same frequency, the resulting intensity at P can be expressed as

$$I = |A_1 + A_2|^2, \tag{1.2}$$

where $A_1 = a_1 exp\ (-i\phi_1)$ and $A_2 = a_2 exp\ (-i\phi_2)$ are the complex amplitudes of the two waves. This results in

$$I = {A_1}^2 + {A_2}^2 + A_1{A_2}^* + {A_1}^*A_2, \tag{1.3}$$

$$I = I_1 + I_2 + 2\sqrt{I_1I_2}cos(\Delta\phi), \tag{1.4}$$

where I_1 and I_2 represent the intensities at P due to each wave independently, and $\Delta\phi = \phi_1 - \phi_2$ denotes the phase difference between them.

If there is an optical path difference $\Delta p = (\lambda/2\pi)\Delta\phi$, defined by an earlier equation, then the interference order N can be written as

$$N = \Delta p/\lambda, \tag{1.5}$$

When the phase difference $\Delta\phi$ between the beams changes linearly across the field of view, the resulting intensity follows a cosine pattern, producing a sequence of alternating bright and dark bands called interference fringes. Each fringe represents a line of constant phase difference, or equivalently, a constant difference in optical path length.

1.2.1 Visibility of interference fringes

In an interference pattern, the intensity reaches its peak value, given by

$$I = I_1 + I_2 + 2\sqrt{I_1I_2}, \tag{1.6}$$

when $\Delta\phi = 2m\pi$ or $\Delta p = m\lambda$, where m is an integer. Conversely, the intensity reaches its minimum value,

$$I = I_1 + I_2 - 2\sqrt{I_1I_2}, \tag{1.7}$$

when $\Delta\phi = (2m+1)\pi$ and $\Delta p = (2m+1)\lambda/2$.

The contrast of the interference fringes, termed visibility V, is defined by

$$V = \frac{I_{max} - I_{min}}{I_{max} + I_{min}}, \tag{1.8}$$

with $0 \leq V \leq 1$. Substituting from the equations for I_{max} and I_{min}, visibility can be expressed as

$$V = \frac{2\sqrt{I_1 I_2}}{I_1 + I_2}, \tag{1.9}$$

The visibility V of interference fringes serves as a measure of the contrast between bright and dark bands within the pattern. A visibility of $V = 1$ indicates perfect contrast, with distinct bright and dark fringes, while lower values of V imply less contrast, resulting in fringes that may appear faint or blurred. High visibility is generally achieved when the intensities I_1 and I_2 of the interfering waves are nearly equal, as this maximizes the term $2\sqrt{I_1 I_2}$ in the visibility equation. Consequently, fringe visibility can provide valuable information about the relative intensities of the interfering beams, which is crucial in applications like precision metrology and holography, where clear, high-contrast fringes are essential for accurate measurements.

1.2.2 Advantages and applications of interferometry

Interferometry is a powerful technique with wide-ranging applications, offering unique advantages in precision measurement, imaging, and materials science. Here are some key benefits, along with references to foundational and contemporary studies in the field:

- **High Precision and Accuracy**: Interferometry can measure distances, displacements, and changes in refractive index with extreme precision, often down to fractions of a wavelength of light. This high sensitivity makes it invaluable for scientific and engineering applications, such as in the precise measurement of optical surfaces and for calibration standards in metrology [5-8].
- **Non-Destructive Testing**: Because interferometry relies on light waves, it allows for contactless measurements, preserving the integrity of delicate or intricate

materials and structures. This feature is essential in quality control and testing of components in aerospace, electronics, and manufacturing, where even slight disturbances could alter the materials properties [9, 10].

- **Enhanced Imaging Resolution**: Interferometric techniques, such as optical coherence tomography and holographic interferometry, can resolve microscopic structures and layers within biological tissues or engineering components. This high-resolution imaging is beneficial in fields like medical diagnostics and semiconductor inspection, providing detailed cross-sectional views without invasive procedures [11, 12].
- **Detection of Small Variations**: Interferometry can detect minimal changes in wavefronts, enabling applications in environmental sensing, seismology, and astronomy. For instance, astronomical interferometry enhances the resolution of telescopes by combining light from multiple telescopes, creating a virtual aperture that reveals finer details in distant celestial bodies [13].
- **Versatility Across Wavelengths and Scales**: Interferometry is adaptable across a wide range of wavelengths, from radio to visible to x-ray, making it useful in both large-scale applications (such as earth observation and astronomy) and nanoscale measurements (like atomic force microscopy). This adaptability allows it to cross disciplines and scales, expanding its applications significantly [14-17].

1.3 Optical vortex and interferometry

An optical vortex is, usually, a coherent beam of light in which the phase of the wavefront spirals around a central point, creating a point of zero intensity, or phase singularity at its centre. In such beams, the phase changes continuously along a circular path around the singularity, resulting in a characteristic helical phase structure. Mathematically, this is often represented using an exponential term, such as $exp(il\theta)$, where θ is the azimuthal angle in cylindrical coordinates, and l denotes the topological charge (TC). The TC l corresponds to the number of 2π-phase windings around the singularity. In optical systems, this TC is directly linked to the orbital angular momentum (OAM) of the beam, where each photon carries an OAM of $l\hbar$, with $\hbar$ being the reduced Planck's constant [18-22]. The ability of optical vortices to carry OAM has opened new possibilities in applications ranging from optical trapping and manipulation to communications and quantum optics. Fig. 1.2 shows the intensity and phase profiles of the optical vortices with different TCs.

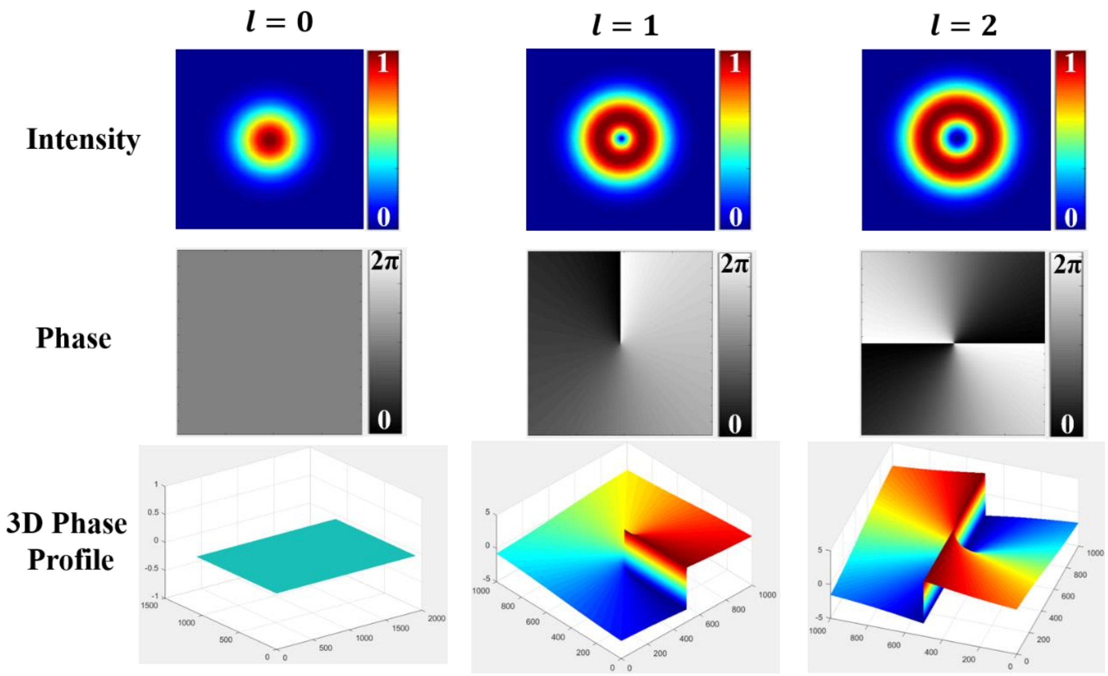

Fig. 1.2 Optical vortices of different topological charge with their intensity, phase and three-dimensional (3D) phase profile.

Interferometry plays a key role in studying and utilizing optical vortices, particularly for characterizing their phase structure and topological properties. In interferometric setups, an optical vortex beam can interfere with a reference beam, typically a plane wave or Gaussian beam, producing distinctive interference patterns. These patterns often appear as a series of forked fringes, where the number of branches corresponds to the TC of the vortex. Such interferometric measurements are crucial for verifying the properties of vortices, including the distribution of phase and intensity, and determining the angular momentum carried by the beam. Therefore, the role of interferometry in detection of optical vortices is discussed in the upcoming section.

1.3.1 Generation of an optical vortex

Optical vortex beams, characterized by their helical phase front and central phase singularity, can be created by shaping the spatial phase structure of light. This tailored phase imparts the beam with OAM, and a range of techniques are available for generating these unique beams. Some of these techniques are discussed below.

1.3.1.1 Spiral phase plate

One of the most effective and widely used methods to generate optical vortices is through the use of a spiral phase plate (SPP). A SPP is a specially designed optical element that introduces a phase shift that varies azimuthally across the beam, creating a vortex phase structure [23, 24]. When a monochromatic light beam, such as from a laser, passes through a SPP, the phase of the light is altered in a manner that varies with the angle θ. The phase variation across the beam's cross-section is given by the SPP's geometry as shown in Fig. 1.3. For each azimuthal angle θ, the phase shift increases linearly, resulting in a beam with a helical phase, where the center of the beam (the optical axis) exhibits zero intensity (a dark spot).

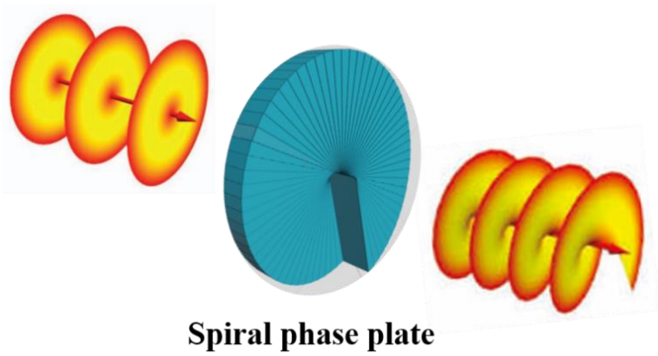

Fig. 1.3 Schematic of the generation of an optical vortex beam with SPP.

1.3.1.2 Mode converters

Mode converters reshape a Gaussian laser mode into a helical mode by modifying the spatial characteristics of the light's wavefront. Beijersbergen et al. designed astigmatic elements that preserve the mode structure, effectively enabling them to act as mode converters for beams with OAM [25]. In 1999, Allen and colleagues further developed a matrix framework to describe the transformation of phase and intensity patterns for monochromatic beams carrying OAM [26]. This model was specifically based on a set of orthogonal laser modes, the Hermite-Gaussian (HG) modes. O'Neil and Courtial later derived this matrix approach in full, expanding the theoretical groundwork for a mode conversion in laser optics [27].

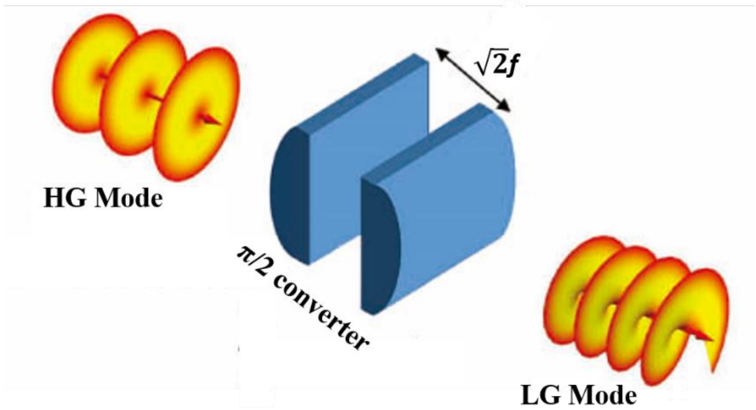

Fig. 1.4 Schematic of the generation of an optical vortex beam with $\pi/2$ converter.

One practical mode converter setup consists of two cylindrical lenses, each with focal length f, arranged at a separation of $\sqrt{2}f$ as shown in Fig. 1.4. This configuration can convert carefully oriented HG beams into Laguerre-Gaussian (LG) beams, altering their spatial structure to include OAM. The transformation enables a straightforward switch between the modes by assigning values m and n (with $m \pm n$ defining the azimuthal mode index) and fixing $p = min(m, n)$, acting analogously to a quarter-wave plate for polarization. This mode conversion process does not alter the mode order, $N = m + n = 2p$, ensuring the energy distribution across the beam remains stable [28, 29].

1.3.1.3 Spatial light modulator

The use of optical elements like SPPs are typically designed to produce vortex beams with a fixed TC, limiting their experimental flexibility. This limitation is addressed by employing digital devices like commercial spatial light modulators (SLMs). The generation of optical vortices using SLMs is a versatile technique due to the ability of SLMs to dynamically control the phase and amplitude of light. An SLM is typically a liquid crystal device that can control the phase of light pixel-by-pixel in response to an applied voltage. By adjusting the orientation of its liquid crystal molecules, the SLM can modulate the spatial properties of an incoming coherent light beam [30]. Using the SLM as shown in Fig. 1.5, a computer-generated hologram (CGH) or a phase pattern with a specific transmittance function can be displayed, where each pixel's phase is individually set according to the hologram's values in two-dimensional space. To produce a helical beam, specific holographic patterns—such as spiral phase holograms, l-fold forked holograms,

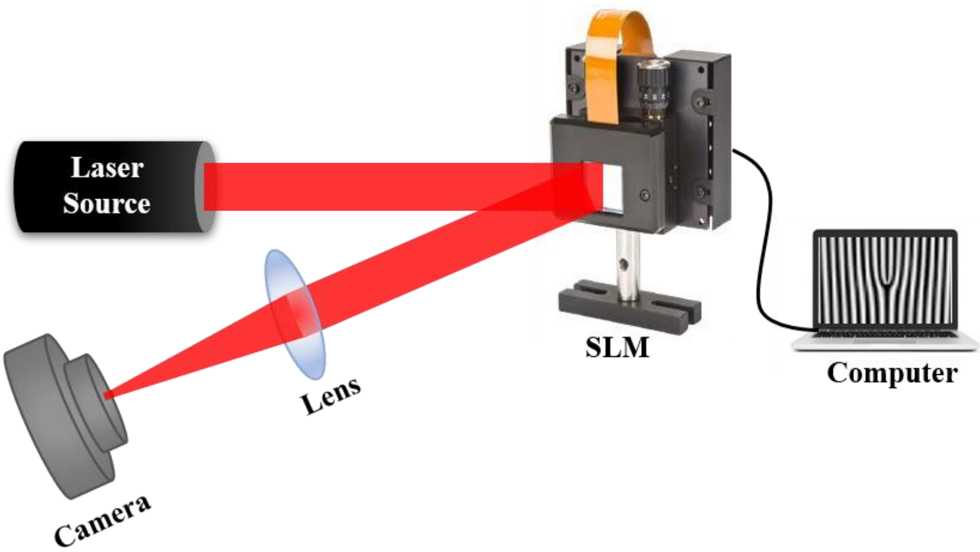

Fig. 1.5 Schematic of the generation of an optical vortex beam using SLM.

and binarized l-fold forked holograms—are projected onto the SLM surface to shape the wavefront of an incoming laser beam to produce optical vortices [31-33]. In addition to SLMs, digital micromirror devices (DMDs) offer a robust alternative for digitally generating vortex beams [34, 35]. These devices provide precise control over incident light with exceptionally high frame rates and extensive spatial degrees of freedom. A DMD consists of an array of microscopic, independently controllable aluminium mirrors that function as high-speed digital switches [34]. Each mirror corresponds to a pixel and can be modulated independently, enabling the dynamic shaping of light fields with great flexibility. This pixel-level control makes DMDs an attractive choice for applications requiring rapid and precise beam manipulation [36]. Thus, these digital tools SLMs and DMDs offer versatility by enabling dynamic control over the generated beam's phase and amplitude, allowing researchers to create optical vortex beams with tunable TCs efficiently and conveniently.

The other methods to generate optical singularities involve diffraction optical elements like fork grating [37-39], q-plates [40, 41], Fermat's spiral [42, 43], pinhole plates [44-46], metasurfaces [47, 48], etc.

1.3.1.4 Direct generation from laser cavity

Optical vortices, characterized by their helical wavefronts and OAM, can be generated within laser cavities by modifying the resonator structure to impose a spiral phase on the emitted beam. These modifications produce beams with phase singularities and a well-defined TC. Intra-cavity generation methods for structured light beams offer compact designs, high efficiency, and superior beam purity compared to extra-cavity methods. Various techniques have been employed for such generation. Generating structured light beams through intra-cavity methods relies on balancing gain and loss across the light field within the laser resonator. A significant approach involves pump shaping, where the pump light field is manipulated to produce structured beams. For instance, Chen et al. used a ring-shaped pump field to generate vector vortex beams with tunable TCs ranging from 0 to 14, ensuring excellent beam quality [49]. Similarly, Ma et al. employed an annular pump beam focused on Nd: GdVO4 crystals to produce Laguerre-Gaussian modes efficiently [50].

Another method entails modifying the phase, amplitude, or polarization within the cavity. Structured light beams can be achieved using resonator mirrors, SPPs, or cavity-inserted elements like SLMs and metasurfaces. For example, Li et al. generated a vortex beam array by applying a Dammann grating hologram onto an SLM, achieving high diffraction efficiency and uniform intensity profiles [51]. Yao et al. introduced spherical aberration by incorporating lenses into the cavity, enhancing mode selection and generating high-order vortex beams [52].

The third approach involves concurrent modulation of the pump and intra-cavity light fields. Wang et al. designed a Z-shaped cavity with off-axis pumping and astigmatism control to produce Hermite-Gaussian and Laguerre-Gaussian modes [53]. Fu et al. advanced this technique by employing dual-off-axis pumping in Yb:CaGdAlO4 lasers to achieve stable higher-order modes and adjustable wavelengths, as well as dual-wavelength vortex beams [54, 55]. Recent innovations using SLMs and metasurfaces have further enabled direct intra-cavity generation of structured light beams with enhanced control and efficiency [56, 57].

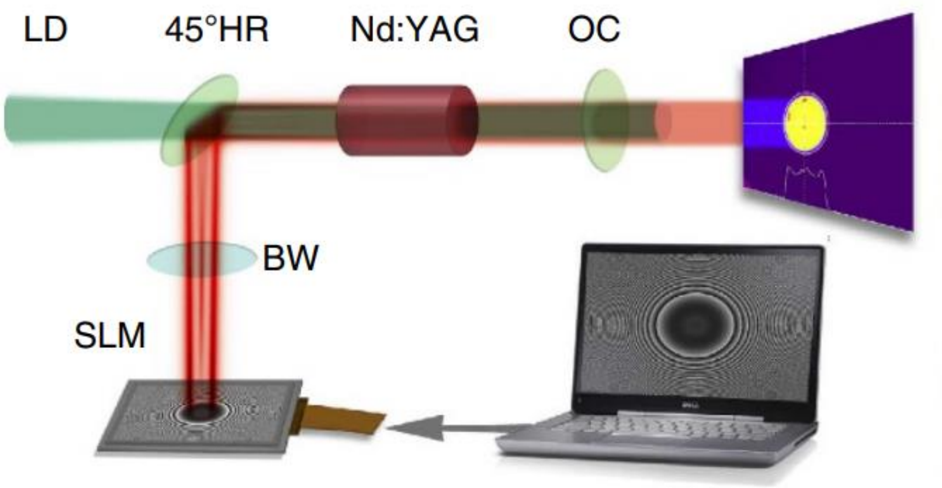

Fig. 1.6 Intra-cavity laser beam shaping using SLM [63].

Fig. 1.6 shows the first intra-cavity digital laser introduced by Ngcoba et al. in 2013, which leveraged a SLM as the back mirror within a laser resonator [58]. This innovation enabled the generation of structured beams with a variety of modes by digitally loading holograms onto the SLM. Depending on the modulation strategy, distinct beam types were achieved. For example, amplitude modulation facilitated the generation of Hermite-Gaussian (HG_{n0}) and Laguerre-Gaussian (LG_{0n}) modes, while phase modulation produced flat-top and airy beams. Additionally, simultaneous amplitude and phase modulation enabled the creation of higher-order Laguerre-Gaussian (LG_{n0}) modes. This flexibility in beam shaping, along with the digital control of beam properties, marked a significant advancement in laser technology and its applications.

1.3.2 Detection of an optical vortex

There are numerous methods developed for analyzing optical vortices, each tailored to capture the unique characteristics of these beams, such as their helical phase structure, OAM, and TC. Accurate analysis of optical vortices is essential in applications like optical communication, quantum information processing, and advanced imaging techniques. Below, we outline some commonly used methods to study and characterize optical vortices.

1.3.2.1 Interferometric techniques

Interferometric methods are highly effective for detecting optical vortices, as they reveal phase dislocations and enable the identification of a vortex's TC. One commonly used technique is the Mach-Zehnder interferometer as shown in Fig. 1.7, where the optical vortex beam interferes with a reference plane wave, resulting in a fork-like fringes in the interference pattern at the camera plane [59]. The interference pattern resembles a forked grating with fringes that exhibit an l-dislocation. These fringes correspond directly to the vortex's TC, making this method a straightforward and precise detection approach. The fringe orientation is influenced by the sign of the TC, allowing efficient estimation of the OAM of the helical beam.

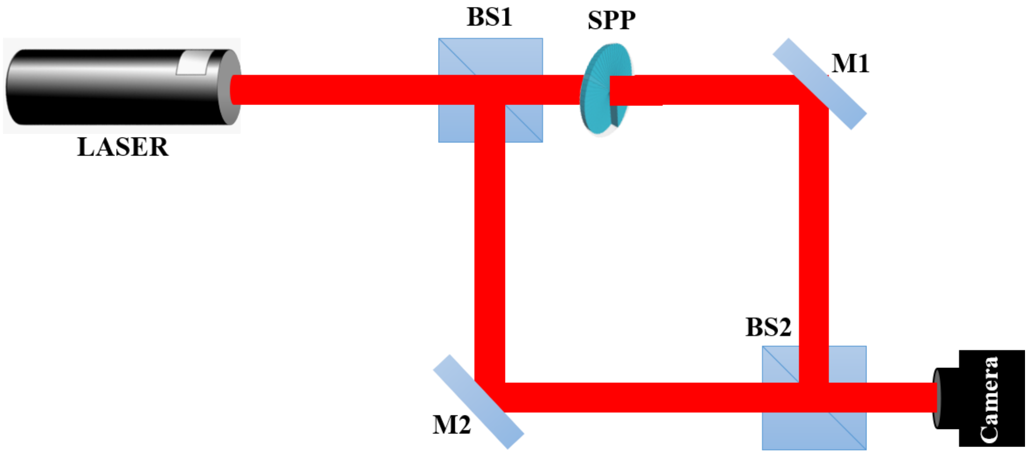

Fig. 1.7 Schematic of the Mach-Zehnder interferometer for measurement of an optical vortex beam. BS: Beam splitter, M: mirror, SPP: spiral phase plate.

Another widely applied interferometric method involves the Young's double-slit setup. The classic Young's double-slit experiment, celebrated as one of the most elegant in physics, can effectively reveal the phase structure of optical vortices (OVs) [60, 61]. For this, the slit length must match the beam waist of the incoming vortex. By employing Young's double slits, one can measure the azimuthal index l of the vortex beam, even for polychromatic vortices from broadband supercontinuum (SC) sources [62].

The interference between a spherical beam and a helical beam generates helical fringes, with the number of fringes corresponding to the TC l [63, 64]. Vortex beams can also be characterized by interfering them with their mirror images [65, 66]. Upon reflection, the vortex beam's rotational direction reverses, resulting in a TC of $-l$. When the original and reflected beams interfere, the pattern formed exhibits a characteristic $2l$-petal structure, offering a direct visual representation of the beam's OAM. Various other interferometric techniques are also employed to analyze optical vortices, including the use of dynamic angular double slits [67, 68], a lateral shear interferometer [69, 70], and an enhanced multipoint interferometer [71].

1.3.2.2 Diffraction techniques

Diffraction techniques are widely employed in measuring optical vortices by analyzing the diffraction patterns created by an optical vortex when it passes through specific apertures or gratings. The unique characteristics of optical vortices, such as their helical phase structure and OAM, lead to distinct diffraction signatures that provide insights into the TC and phase properties of the beam.

The measurement of helical beams using diffraction techniques can be categorized into three main methods: aperture diffraction, grating diffraction, and cylindrical lens diffraction.

- **Aperture Diffraction**: When a helical beam passes through apertures of various shapes, such as triangular or square, it generates a distinct diffraction pattern in the far-field. This diffraction pattern can be used to measure the TC of the helical beam [72-74]. The first demonstration of vortex beam diffraction through an aperture was presented by Hickmann et al. [72]. Various aperture shapes, including circular [75], diamond-shaped [76], hexagonal [77], and regular polygons [78], have been utilized in diffraction experiments to detect helical beams.

- **Grating Diffraction**: Grating diffraction is another effective method for measuring optical vortices. The vortex beam interacts with a diffraction grating, and the resulting diffraction pattern provides valuable information about the beam's TC. The grating diffraction method has been widely used in vortex beam analysis [79-81].

- **Cylindrical Lens Diffraction**: Cylindrical lenses are also commonly used for vortex beam detection. When the helical beam passes through a cylindrical lens, it undergoes a phase transformation, and the diffraction pattern is altered in a way that allows for the determination of the vortex's TC [28, 29, 82, 83].

Fig. 1.8 shows results for the diffraction using different techniques. These diffraction-based methods offer reliable techniques for measuring optical vortices and their TC. Other techniques for the detection of OVs involve methods like geometric coordinate transformation [84, 85], deep learning [86-88], surface plasmon polaritons [89-91], etc.

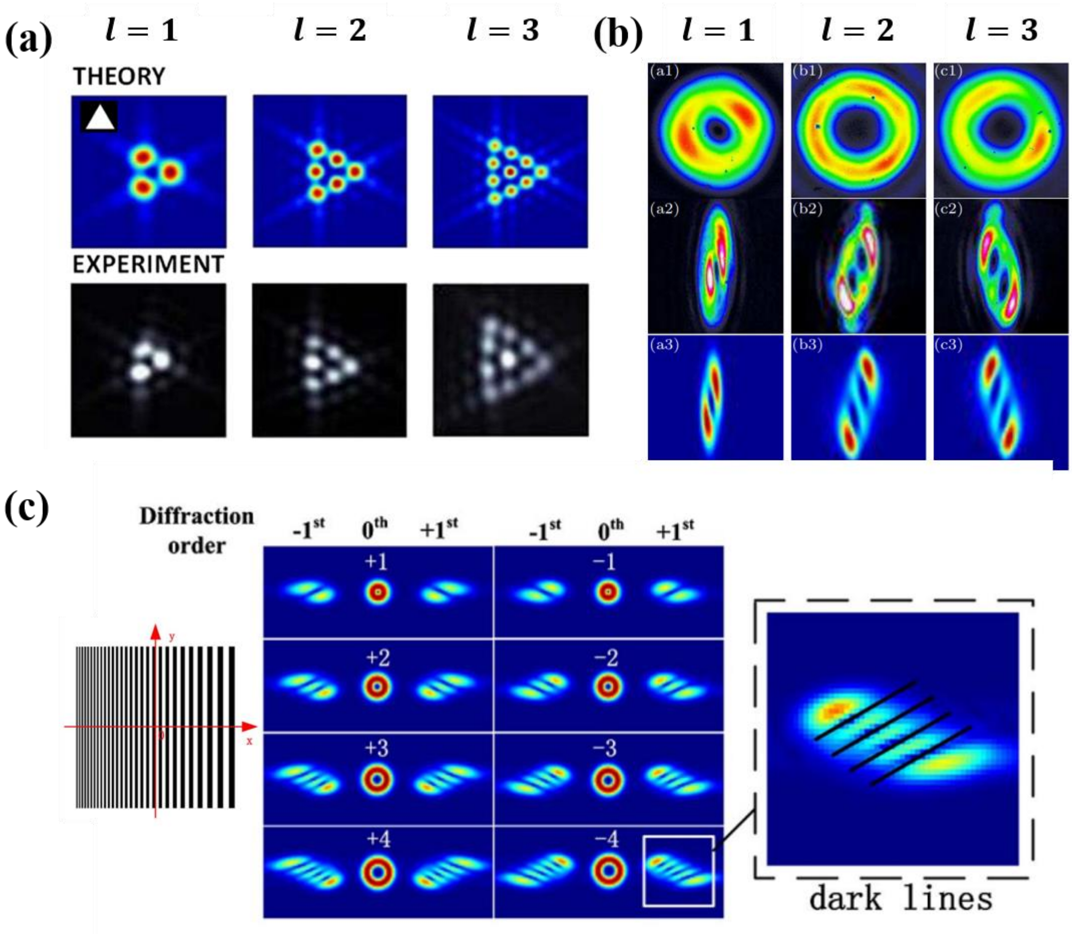

Fig. 1.8 Diffraction patterns: (a) Aperture diffraction method: triangular aperture [72], (b) Cylindrical lens diffraction method [82], (c) Grating diffraction method: gradually changing period grating [80].

1.3.3 Application of optical vortices

1.3.3.1 Particle trapping

Conventional Gaussian beam-based traps cannot trap highly reflective particles, such as metallic ones, and are prone to optical damage due to the high intensity near the beam's focal point. Phase singular beams, however, can overcome these limitations. These beams are particularly effective in trapping metallic particles in their annular region, where radiation pressure is weaker. Thus, optical vortices are used to trap particles due to their inherent OAM. The helical wavefronts of vortex beams can exert a torque on particles, as well as a radial force, making them ideal for trapping and rotating micro and nanoparticles. Trapping microscopic particles is crucial in fields like biology, biophysics, and acoustics.

The concept of trapping small dielectric particles using laser beams was first introduced by Ashkin in the early 1970s [92]. Initial experiments employed two counter-propagating Gaussian laser beams, which trapped a particle of high refractive index at their intersection. The particle was held in place by the transverse gradient force, while the opposing radiation pressure forces balanced it at the equilibrium point between the beams' foci [93]. In optical levitation, a single Gaussian laser beam directed upward supports the particle against gravity using radiation pressure. The transverse gradient force keeps the particle centered in the beam. By tightly focusing the Gaussian beam with a high numerical aperture microscope objective, a 3D gradient field is created, allowing trapping in optical tweezers [94]. In this case, the tight focus generates both transverse and axial gradient forces. These forces result in the axial movement of the particle toward the focus, where it remains stably trapped.

Fig. 1.9 shows a standard optical tweezers setup operates by tightly focusing a laser beam to create a diffraction-limited spot for trapping particles [95]. The setup begins with a collimated laser beam expanded to overfill the back aperture of a high numerical aperture (NA) microscope objective. The expanded beam is reflected toward the objective using a dichroic mirror (DM), which allows precise focusing of the laser inside a sample chamber to trap particles. For imaging, white light from an LED illuminate the sample, and the forward-scattered light from trapped particles is collected by a condenser lens. This light is then projected onto a quadrant photodetector (QPD) through back focal plane interferometry, enabling accurate tracking of particle motion. By analyzing the intensity signals across the QPD's four quadrants, the system measures the axial position and other dynamics of the trapped particles with high precision. This configuration ensures robust trapping and sensitive detection, making it invaluable for micro- and nano-scale manipulation studies [95].

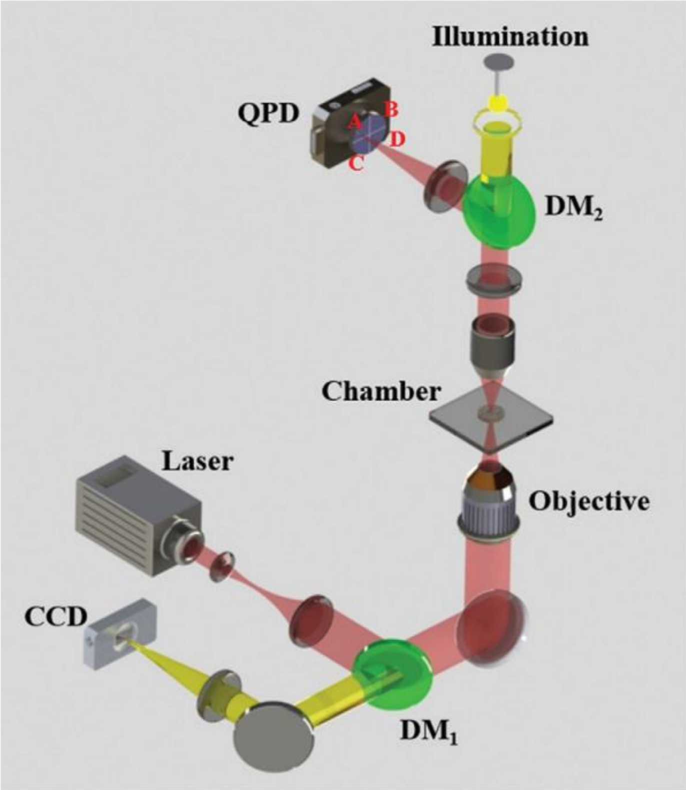

Fig. 1.9 Schematic of experimental configuration of conventional optical tweezers [95].

1.3.3.2 Optical communication

Optical vortices have gained significant attention in optical communication due to their potential for increasing the capacity and efficiency of data transmission. The primary advantage of using optical vortices in communication systems lies in the ability to encode information in the OAM of light, allowing for the multiplexing of channels using different OAM states. This is known as OAM multiplexing, which significantly enhances the information-carrying capacity of optical fibers or free-space communication channels [96].

One of the key features of optical vortices is their phase singularity at the center, which results in a helical wavefront. This unique property allows multiple OAM modes to be superimposed on the same wavelength, thus enabling higher-dimensional data encoding. The ability to transmit several independent channels of data simultaneously without interference opens up new possibilities for increasing bandwidth efficiency. This method has been demonstrated in free-space optical communication systems, where the high-dimensional OAM modes can be utilized for simultaneous data streams [97-99].

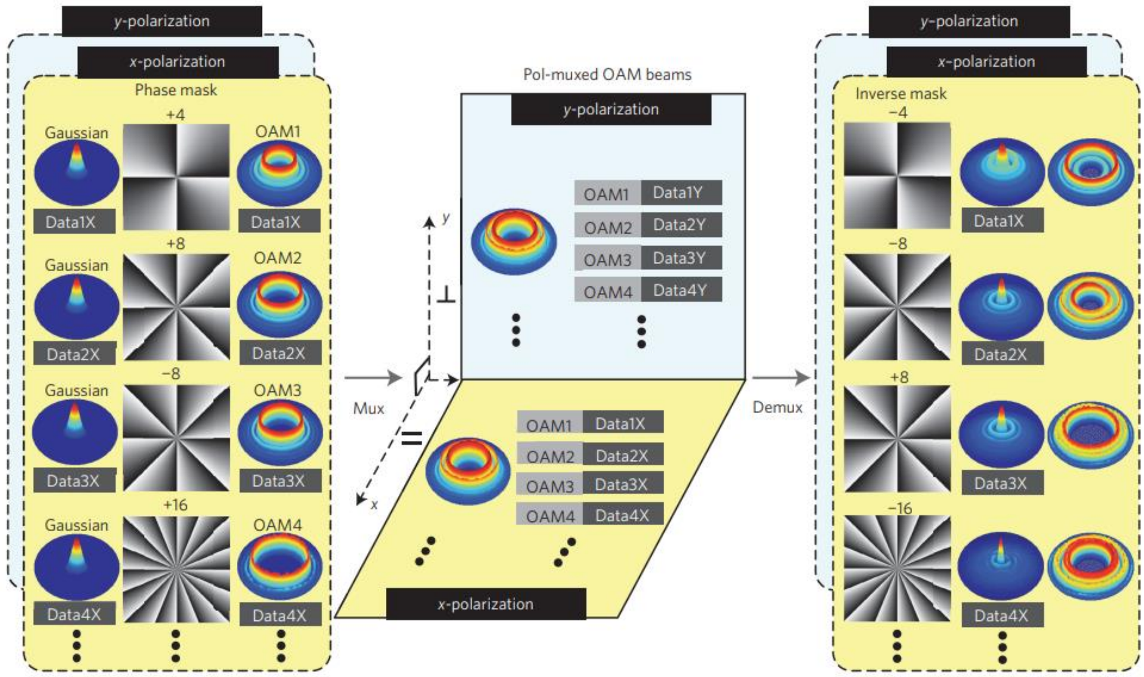

Fig. 1.10 Free-space optical communication using polarization mutiplexing [99].

Figure 1.10 illustrates the concept of free-space optical (FSO) communication utilizing helical modes, as described by Wang et al. [99]. The method uses multiplexing and demultiplexing OAM beams, combined with polarization multiplexing. Thus, this method allows multiple information channels to be transmitted and received simultaneously, enhancing data throughput significantly. In the multiplexing phase, multiple OAM beams with characteristic doughnut-shaped intensity profiles are generated, each corresponding to a specific OAM state. These beams are spatially combined into a single composite beam, enabling efficient channel integration. The beams may also be paired with polarization multiplexing, wherein each OAM channel carries two orthogonal polarization states (e.g., horizontal and vertical), further doubling the channel capacity. Demultiplexing involves separating these combined channels back into individual streams. This is achieved by converting one specific OAM beam into a mode with a high-intensity peak at the center, distinguishing it from the other doughnut-shaped beams. Using spatial filtering techniques, such as custom optical elements or digital processing, the central-intensity beam is isolated, while the remaining OAM channels retain their original profiles for subsequent processing.

1.3.3.3 Spiral interferometry

In most interferometers, light reflected from or transmitted through an object is combined with a uniform reference wave to produce an interference pattern that encodes information about the object's surface height or phase profile. Interferograms of smooth objects typically consist of closed contour lines, each representing a specific height or phase value in terms of the optical wavelength. However, a major limitation of this method is the inability to directly distinguish between surface depressions and elevations in the optical thickness of the sample. To overcome this, fringe demodulation techniques are employed, which involve capturing multiple interferograms with different phase offsets (phase stepping), from varying angles (angular multiplexing), or with different wavelengths (wavelength multiplexing). Spiral interferometry addresses this challenge by using a spiral phase element as a spatial filter. This results in interference fringes that spiral in shape, with the direction of rotation indicating whether the surface is elevated or depressed.

A significant advantage of spiral interferometry [100-102] is that a single exposure can provide enough topographical information to reconstruct the entire phase profile of the object. This is particularly useful for high-speed interferometry, enabling the capture of interferograms with a single laser pulse or for video recording of rapidly changing surfaces, where each video frame can be processed independently. Fig. 1.11 shows a standard interferogram and a spiral interferogram of a simulated phase object. In Fig. 1.11(a), closed interference fringes represent the two extremes of the object’s surface. In Fig. 1.11(b), the spiral pattern, whether clockwise or counterclockwise, indicates that one extreme is a maximum and the other is a minimum.

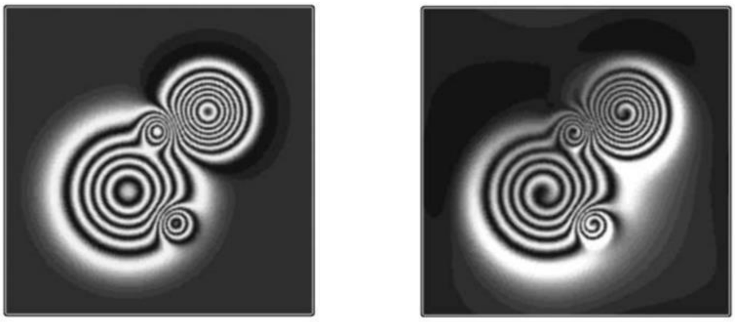

Fig. 1.11 Sample profile of a surface (a) Normal interferogram. (b) Spiral interferogram [100].

Other important applications of OVs involve quantum technology [103, 104], astrometry [105], biomedical applications [106], metrology [107, 108], material processing [109, 110], etc.

1.4 Low coherent source

Fully coherent light, such as laser beams, presents several challenges that impact its applications in optical systems. One of the major issues is its high sensitivity to environmental factors, such as temperature fluctuations and vibrations, which can distort phase and wavefront information, leading to poor image quality or measurement inaccuracies [111, 112]. Additionally, a fully coherent light can generate speckle noise when interacting with rough surface, which degrades the quality of images and measurements in fields like interferometry and holography. Another limitation is the shallow depth of field in imaging systems using coherent light, making it difficult to capture three-dimensional information from a scene or object, particularly in microscopy applications [113]. Furthermore, phase retrieval techniques, often essential in interferometric measurements and holography, are more complex with fully coherent light due to the need for precise phase control.

In contrast, low-coherence light offers several advantages. It is less sensitive to environmental disturbances, providing greater stability in real-world conditions. Additionally, its broader spectrum and shorter coherence length inherently reduce speckle noise, resulting in clearer images and more accurate measurements [114]. Low-coherence light also provides a larger depth of field [115], which is beneficial for three-dimensional imaging and applications like optical coherence tomography (OCT), where depth resolution is essential [116, 117]. Moreover, phase retrieval and interferometric measurements are simpler with low-coherence light, as it requires less precise phase control, which reduces the complexity of optical systems. Finally, low-coherence light is advantageous in imaging through turbid media, such as biological tissues, making it ideal for biomedical applications like OCT [11].

1.5 Concept of optical coherence

When two sources have a constant phase difference, they produce a stable interference pattern. Generally, if two beams originate from the same source, their fluctuations are correlated, classifying them as either fully or partially coherent depending on the degree of correlation. Conversely, beams from separate sources have uncorrelated fluctuations and are thus mutually incoherent. Coherence essentially describes whether two points in a wave maintain a constant phase relationship, and it directly impacts the interference patterns observed when two beams from a source overlap [118]. Initial studies on light's wave nature, such as Hooke's early findings [119], were later advanced by Huygens [120] and Young [121]. Young's double-slit experiment confirmed that light from two pinholes interferes constructively and destructively, highlighting the connection between interference and coherence. The ability of light beams to produce clear interference patterns reflects their coherence, a property not understood during that time. This coherence determines the extent to which different light sources can interfere, forming the foundation of modern optical coherence theories [122].

The concept of coherence developed over time. E. Verdet contributed by studying regions on Earth where sunlight oscillations align [123]. Michelson further investigated the link between interference fringe visibility and intensity distribution but couldn't express this relationship quantitatively with field correlations [124,125]. Later, von Laue formalized these correlations for electric field vibrations, while van Cittert calculated the joint probability of light vibrations across a plane illuminated by an extended source [126, 127]. In 1938, Zernike introduced the "degree of coherence" concept, linking spatial coherence with fringe visibility [128], though he initially overlooked the time lag between beams.

Emil Wolf expanded coherence theory by accounting for time differences, laying the foundation for modern space-time coherence theory [129]. Although analyzing correlation functions with time-retardation factors was challenging, particularly for scattering problems, Wolf reframed coherence theory in the space-frequency domain, explaining phenomena like the spectral line shift due to source correlation, known as the Wolf shift [130-133]. This modernized theory, advanced by Wolf and Mandel, has applications across fields including stellar interferometry, spectroscopy, and imaging.

1.5.1 Types of coherence

Coherence in light can be characterized as either temporal or spatial, based on whether the correlation between electric field fluctuations is examined over time or space. Temporal coherence involves interference between a light beam and a delayed version of itself, without any spatial shift, achieved through amplitude splitting. In contrast, spatial coherence refers to the interference of a light beam with a version of itself that is spatially shifted but not delayed in time, a process known as wavefront splitting.

1.5.1.1 Temporal coherence

Temporal coherence of two beams refers to their capacity to create interference fringes based on their time-delay correlations. For instance, in a Michelson interferometer, the formation of interference fringes is due to the temporal coherence of light beam with bandwidth $\Delta\omega$, interference occurs only if the time delay Δt satisfies the condition [134]

$$\Delta t \Delta\omega \leq 1, \tag{1.10}$$

This time delay, Δt, is known as the coherence time, which corresponds to a path difference $\Delta l = c\Delta t$, where c is the speed of light, known as the longitudinal coherence length. Coherence length can also be expressed as

$$\Delta l \approx \frac{\bar{\lambda}^2}{\Delta\lambda}, \tag{1.11}$$

where $\bar{\lambda}$ represents the mean wavelength of light. Thus, coherence time indicates the duration over which the field retains a definite phase relationship, remaining sinusoidal in form. Thermal light sources, like discharge lamps or incandescent sources with narrow spectral widths, exhibit coherence times of about 10^{-8}s and coherence lengths around 3 m. Stabilized lasers, with frequency spreads of approximately 10^4 Hz, achieve coherence times on the order of 10^{-4}s and coherence lengths up to 30 km.

1.5.1.2 Spatial coherence

Spatial coherence between two beams is their capacity to produce interference fringes due to correlations existing over a spatial separation depends on the source size; for example, in Young's interferometer Fig. 1.12.

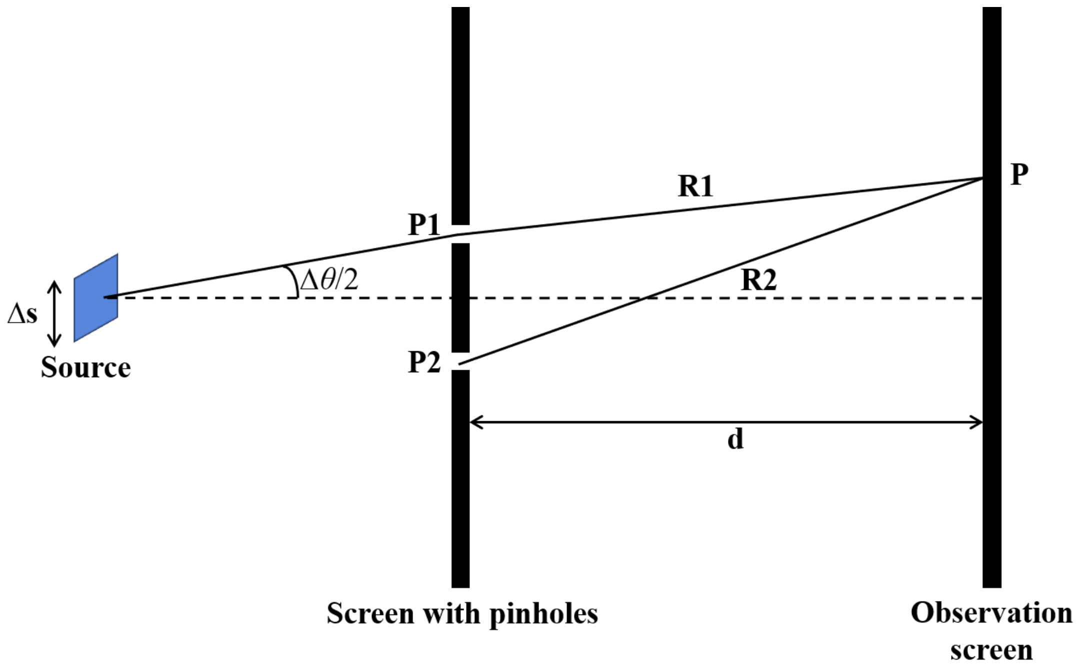

Fig. 1.12 Schematic diagram of the Young's interference experiment.

If $\Delta\theta$ represents the angular separation between two slits as observed from a source, and Δs denotes the size of the source, the condition necessary for the formation of interference fringes can be expressed as an inequality. Therefore, the criterion for fringe formation can be expressed as [134]

$$\Delta\theta\Delta s \leq \bar{\lambda}, \tag{1.12}$$

This inequality establishes a relationship between the angular spread of light from the source and the geometry of the setup. If R is the distance between the source and the pinhole plane, fringes will form within a region around the point whose area, termed the *coherence area*, is given by [134]

$$\Delta A \approx (R\Delta\theta)^2 \approx \frac{R^2\bar{\lambda}^2}{S}, \tag{1.13}$$

where $S = (\Delta s)^2$ represents the source area. The term $R\Delta\theta$, the square root of the coherence area, is the transverse coherence length. Remarkably, even uncorrelated sources can generate field correlations during propagation and superposition.

For quasi-monochromatic light, the coherence volume is defined as the space in which the field remains coherent. It is represented by a right-angle cylinder with a base equal to the coherence area and a height corresponding to the longitudinal coherence length [134]. This coherence volume, given by

$$\Delta V = \Delta A \Delta l \approx \frac{R^2 \bar{\lambda}^4}{S \Delta \lambda}, \tag{1.14}$$

represents the spatial region where photons are indistinguishable, providing strong fringe contrast in interference experiments.

1.5.2 Interference of arbitrary light source

Let $U(\boldsymbol{r}, t)$ represent the amplitude of the optical field at point P (Fig. 1.12), designated by the position vector $\boldsymbol{r}$ at time t, where the field is quasi-monochromatic—meaning the light's effective bandwidth is small relative to its mean frequency. The cross-correlation function, which depends on two-time arguments only through their difference, is termed the mutual coherence function (MCF) and is defined as [134, 135]

$$\Gamma(\boldsymbol{r}_1, \boldsymbol{r}_2, \tau) = \langle U^*(\boldsymbol{r}_1, t) U(\boldsymbol{r}_2, t+\tau) \rangle = \lim_{T \to \infty} \frac{1}{2T} \int_{-T}^{T} U^*(\boldsymbol{r}_1, t) U(\boldsymbol{r}_2, t+\tau)\, dt, \tag{1.15}$$

where $\tau = t_1 - t_2 = \frac{R_1 - R_2}{c}$. Here, τ represents the time difference based on the path difference between points R_1 and R_2, and c is the speed of light. The instantaneous intensity I at point P and at time t is given by $I = \langle U^*(\boldsymbol{r}_1, t) U(\boldsymbol{r}_2, t) \rangle$. The normalized form of MCF is expressed as

$$\gamma(\boldsymbol{r}_1,\boldsymbol{r}_2,\tau)=\frac{\Gamma(\boldsymbol{r}_1,\boldsymbol{r}_2,\tau)}{\sqrt{\Gamma(\boldsymbol{r}_1,\boldsymbol{r}_1,0)\,\Gamma(\boldsymbol{r}_2,\boldsymbol{r}_2,0)}}, \tag{1.16}$$

where $\Gamma(\boldsymbol{r}_i,\boldsymbol{r}_i,0)$ (for $i=1,2$) denotes the self-coherence or intensity at each point in the source plane. The intensity at point P can thus be expressed as

$$I(\boldsymbol{r},t)=I(\boldsymbol{r}_1,t)+I(\boldsymbol{r}_2,t)+2\sqrt{I(\boldsymbol{r}_1,t)I(\boldsymbol{r}_2,t)}|\gamma(\boldsymbol{r}_1,\boldsymbol{r}_2,\tau)|\cos[\alpha(\boldsymbol{r}_1,\boldsymbol{r}_2,\tau)-\delta], \tag{1.17}$$

where $\alpha(\boldsymbol{r}_1,\boldsymbol{r}_2,\tau)=arg(\gamma(\boldsymbol{r}_1,\boldsymbol{r}_2,\tau))+\omega\tau$ and $\delta=\frac{\omega(R_1-R_2)}{c}$ depends on the path difference, with ω being the angular frequency of light. This expression describes the interference behavior of a statistically stationary scalar optical field.

The visibility $V(\boldsymbol{r})$ of the interference fringes at point P serves as a measure of contrast and is given by

$$V(\boldsymbol{r})=\frac{I_{max}(\boldsymbol{r})-I_{min}(\boldsymbol{r})}{I_{max}(\boldsymbol{r})+I_{min}(\boldsymbol{r})}, \tag{1.18}$$

where $I_{max}(\boldsymbol{r})$ and $I_{min}(\boldsymbol{r})$ are the maximum and minimum intensity values around point P. For equal intensities of the two beams, visibility simplifies to

$$V(\boldsymbol{r})=|\gamma(\boldsymbol{r}_1,\boldsymbol{r}_2,\tau)|, \tag{1.19}$$

indicating that $|\gamma(\boldsymbol{r}_1,\boldsymbol{r}_2,\tau)|$ quantifies fringe visibility, constrained by $0\leq|\gamma(\boldsymbol{r}_1,\boldsymbol{r}_2,\tau)|\leq 1$. In the case $|\gamma(\boldsymbol{r}_1,\boldsymbol{r}_2,\tau)|=1$, complete coherence is achieved, and the intensity variation at P is maximal when $\alpha(\boldsymbol{r}_1,\boldsymbol{r}_2,\tau)-\delta=\left(n+\frac{1}{2}\right)\pi$ (where $n=0,\pm1,\pm2\ldots$). Conversely, $|\gamma(\boldsymbol{r}_1,\boldsymbol{r}_2,\tau)|=0$ signifies complete incoherence, resulting in uniform intensity with no fringe formation. Values between 0 and 1 indicate partial coherence, where intensity fluctuates periodically varying between $2(1+|\gamma(\boldsymbol{r}_1,\boldsymbol{r}_2,\tau)|)$ and $2(1-$

$|\gamma(\boldsymbol{r}_1, \boldsymbol{r}_2, \tau)|$) times the intensity contributed by an individual beam as shown in Fig. 1.13. The parameter $\gamma(\boldsymbol{r}_1, \boldsymbol{r}_2, \tau)$ is thus known as the complex degree of coherence, linking fringe contrast to coherence between the beams.

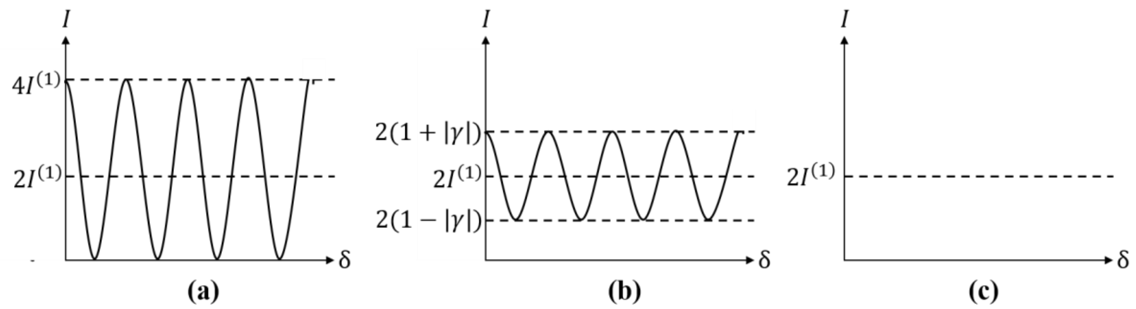

Fig. 1.13 The average intensity distribution (a) coherent superposition (b) partially coherent superpositon (c) incoherent superposition [134].

The above formulation of interference law is in space-time domain. However, there exists an alternative framework in the space-frequency domain, which is particularly advantageous for analyzing the behavior of quasi-monochromatic radiation in dispersive or absorbing media. This domain centers on the cross-spectral density (CSD) function, $W(\boldsymbol{r}_1, \boldsymbol{r}_2, \omega)$, which serves as the Fourier transform of the mutual coherence function $\Gamma(\boldsymbol{r}_1, \boldsymbol{r}_2, \tau)$. Mathematically, this relationship is expressed as [134]

$$W(\boldsymbol{r}_1, \boldsymbol{r}_2, \omega) = \frac{1}{2\pi}\int_{-\infty}^{\infty} \Gamma(\boldsymbol{r}_1, \boldsymbol{r}_2, \tau) e^{i\omega\tau} d\tau, \tag{1.20}$$

The CSD function itself represents a correlation function, statistically averaging the product of electric field amplitudes at different frequencies. It is defined as:

$$W(\boldsymbol{r}_1, \boldsymbol{r}_2, \omega) = \langle U^*(\boldsymbol{r}_1, \omega) U(\boldsymbol{r}_2, \omega)\rangle, \tag{1.21}$$

where the angular brackets indicate ensemble averaging.

From this function, the spectral density $S(\boldsymbol{r}, \omega)$, or intensity at a frequency ω, at any point $P(\boldsymbol{r})$ is derived as

$$S(\boldsymbol{r},\omega) = W(\boldsymbol{r},\boldsymbol{r},\omega) = \langle |E(\boldsymbol{r},\omega)|^2 \rangle, \tag{1.22}$$

The concept of interference extends naturally into the spectral domain, leading to the spectral interference law. This is analogous to the interference law in the space-time domain but accounts for frequency-specific coherence properties. The law is expressed as

$$S(\boldsymbol{r},\omega) = S(\boldsymbol{r}_1,\omega) + S(\boldsymbol{r}_2,\omega) + 2\sqrt{S(\boldsymbol{r}_1,\omega)S(\boldsymbol{r}_2,\omega)}|\mu(\boldsymbol{r}_1,\boldsymbol{r}_2,\omega)|cos[\beta(\boldsymbol{r}_1,\boldsymbol{r}_2,\omega)], \tag{1.23}$$

where $\mu(\boldsymbol{r}_1,\boldsymbol{r}_2,\omega)$ is the spectral degree of coherence, and $\beta(\boldsymbol{r}_1,\boldsymbol{r}_2,\omega)$ represents the phase difference between fields at points $P_1(\boldsymbol{r}_1)$ and $P_2(\boldsymbol{r}_2)$.

The spectral degree of coherence, a normalized measure of the correlation between fields at these points, is given by

$$\mu(\boldsymbol{r}_1,\boldsymbol{r}_2,\omega) = \frac{W(r_1,r_2,\omega)}{\sqrt{W(r_1,r_1,\omega)\,W(r_2,r_2,\omega)}}, \tag{1.24}$$

This parameter lies between 0 and 1, where $|\mu(\boldsymbol{r}_1,\boldsymbol{r}_2,\omega)| = 0$ indicates complete spectral incoherence, and $|\mu(\boldsymbol{r}_1,\boldsymbol{r}_2,\omega)| = 1$ signifies perfect spectral coherence.

1.5.3 Generation of spatial coherence on propagation

For a broad incoherent source, each point on its surface acts as an independent emitter of light. As light propagates, the field at any two points in space results from the cumulative fields emitted by these independent sources. With increasing propagation distance, the fields at any two nearby points become more similar due to the averaging effect of multiple overlapping waves, as depicted in Fig. 1.14.

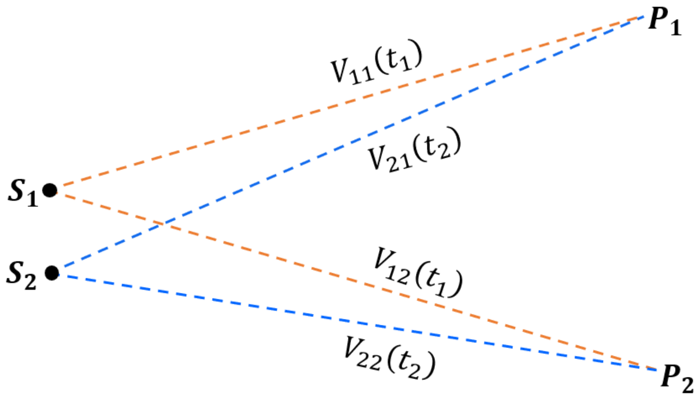

Fig. 1.14 Illustration demonstrating the emergence of spatial coherence during propagation.

The total electric field amplitudes, $V(P_1)$ and $V(P_2)$, at two points P_1 and P_2 can be expressed as the vector sum of contributions from sources S_1 and S_2 [134], such that

$$V(P_1) = V_{11}(t_1) + V_{21}(t_2), V(P_2) = V_{12}(t_1) + V_{22}(t_2), \tag{1.25}$$

where fields $V_{11}(t_1)$ and $V_{12}(t_1)$; and $V_{21}(t_2)$ and $V_{22}(t_2)$ become correlated. As a result, the fields $V(P_1)$ and $V(P_2)$ also become correlated, demonstrating a gain in spatial coherence upon propagation. Therefore, the coherence of light can significantly change during propagation, as explained by the theory of partial coherence. This change occurs because the mutual coherence function adheres to two precise propagation laws, each represented by a wave equation in free space. These are expressed as

$$\nabla_i^2 \Gamma(\boldsymbol{r}_1, \boldsymbol{r}_2, \tau) = \frac{1}{c^2}\frac{\partial^2}{\partial \tau^2}\Gamma(\boldsymbol{r}_1, \boldsymbol{r}_2, \tau), \text{ for } i = 1, 2, \tag{1.26}$$

where ∇_i^2 are the Laplacian operators applied to the points $\boldsymbol{r}_1$ and $\boldsymbol{r}_2$, for the CSD function, the Fourier transform of this equation leads to the Helmholtz equations in free space, given by [134]

$$\nabla_i^2 W(\boldsymbol{r}_1, \boldsymbol{r}_2, \omega) + k^2 W(\boldsymbol{r}_1, \boldsymbol{r}_2, \omega) = 0, \text{ for } i = 1, 2, \tag{1.27}$$

where $k = \omega/c$. In the incoherent source, there is initially no correlation between the fields at different points. However, as light propagates, each point in the field receives contributions from all points of the source, so at a sufficient distance, the fields at closely spaced points become similar as they receive light from nearly the same regions of the source. This coherence gain during propagation is the basis of the van Cittert-Zernike theorem, which describes how spatial coherence emerges over distance.

1.5.4 The van Cittert-Zernike theorem

To examine the correlations generated in the field produced by an extended planar source of natural light, let us assume the source is statistically stationary (in the wide sense) and emits radiation within a narrow frequency range $\Delta\omega$ around a central frequency $\bar{\omega}$. Additionally, we assume that the source's dimensions are small compared to the distances from the source to observation points P_1 and P_2, and that the angles formed by lines from source points to P_1 and P_2 with normal to the source are also small (see Fig. 1.15).

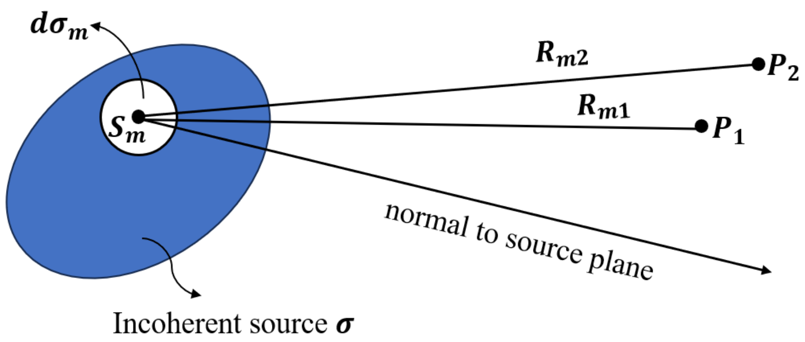

Fig. 1.15 Spatial coherence generation from an incoherent source [134].

Imagine dividing the source into small elements $d\sigma_1$, $d\sigma_2$,…, $d\sigma_m$ centered at points S_1, S_2,…, S_m, where the element sizes are much smaller than the mean wavelength λ of the emitted light. Let $U_{m1}(t)$ and $U_{m2}(t)$ represent the complex amplitudes of the fields at points P_1 and P_2, respectively, contributed by the source element $d\sigma_m$. The total complex field amplitudes at P_1 and P_2 are then given by [134]

$$U_1(t) = \sum_m U_{m1}(t) \, , U_2(t) = \sum_m U_{m2}(t), \quad (1.28)$$

In the context of spatial coherence, the mutual intensity function provides a measure of the correlation between the complex amplitudes of an optical field at two points, P_1 and P_2, at a given time. When time delay τ is taken to be zero, as is often the case in symmetric experimental setups or for optical systems near the optical axis, the mutual intensity $J(P_1, P_2)$ simplifies to

$$J(P_1, P_2) = \Gamma(P_1, P_2, 0) = \langle U_1^*(t) U_2(t) \rangle$$

$$= \sum_m \langle U_{m1}^*(t) U_{m2}(t) \rangle + \sum_{m \neq n} \sum \langle U_{m1}^*(t) U_{n2}(t) \rangle, \quad (1.29)$$

Assuming the source generates natural (incoherent) light, the contributions from different source elements are uncorrelated and have zero mean. Thus, the double summation term vanishes when $m \neq n$.

$$\sum_{m \neq n} \sum \langle U_{m1}^*(t) U_{n2}(t) \rangle = \sum_{m \neq n} \sum \langle U_{m1}^*(t) \rangle \langle U_{n2}(t) \rangle = 0, \quad (1.30)$$

For field points P_1 and P_2 located at distances R_{m1} and R_{m2} from the source element $d\sigma_m$, we can express the field from $d\sigma_m$ as

$$U_{m1}(t) = \frac{A_m(t - R_{m1}/c)}{R_{m1}} exp[-i\overline{\omega}(t - R_{m1}/c)], \quad (1.31)$$

$$U_{m2}(t) = \frac{A_m(t - R_{m2}/c)}{R_{m2}} exp[-i\overline{\omega}(t - R_{m2}/c)], \quad (1.32)$$

where $|A_m|$ represents the strength, and arg A_m the phase of radiation emitted by $d\sigma_m$, c represents the speed of light in vacuum.

By substituting into the mutual intensity equation and assuming stationarity, we obtain

$$J(P_1, P_2) = \sum_m \frac{\langle A_m^*(t - R_{m1}/c) A_m(t - R_{m2}/c) \rangle}{R_{m1} R_{m2}} exp[i\overline{\omega}(R_{m2} - R_{m1})/c], \quad (1.33)$$

$$J(P_1, P_2) = \sum_m \frac{\langle A_m^*(t) A_m[t-(R_{m2}-R_{m1})/c] \rangle}{R_{m1}R_{m2}} exp[i\bar{\omega}(R_{m2} - R_{m1})/c], \quad (1.34)$$

When the path differences $R_{m2} - R_{m1}$ are small relative to the coherence length of the light, retardation terms $(R_{m2} - R_{m1})/c$ can be neglected, yielding

$$J(P_1, P_2) = \sum_m \frac{\langle A_m^*(t) A_m(t) \rangle}{R_{m1}R_{m2}} exp[i\bar{\omega}(R_{m2} - R_{m1})/c], \quad (1.35)$$

Let $I(S)$ represent the intensity emitted per unit area from the source. Accordingly, we can approximate $\langle A_m^*(t) A_m(t) \rangle \approx I(S) d\sigma_m$. With a large number of source elements, the source can be treated as continuous, leading to replace submission with an integral expression for mutual intensity

$$J(P_1, P_2) = \int_\sigma \; I(S) \frac{exp[i\bar{k}(R_2-R_1)/c]}{R_1R_2} dS, \quad (1.36)$$

where R_1 and R_2 are the distances from a typical source point S to the observation points P_1 and P_2, respectively. This formulation represents the van Cittert-Zernike theorem, which states that the spatial coherence in the observation plane is the two-dimensional spatial Fourier transform of the intensity distribution across the incoherent source aperture.

1.5.5 Measurement of spatial coherence

There are numerous techniques available for measuring the spatial coherence of light, each tailored to specific experimental conditions and objectives. In this section, we will discuss a selection of these methods, emphasizing their principles, and unique advantages in characterizing the coherence state of optical fields.

These methods generally fall into categories based on their underlying principles, such as aperture-based systems, SLM-based configurations, pinhole methods, or interferometric techniques. Each approach has its strengths, depending on factors like precision, experimental simplicity, and suitability for dynamic or complex fields. We will explore these methodologies to understand their roles in the measurement of spatial coherence of light.

1.5.5.1 Young's interferometer

In *Principles of Optics* [135], Born and Wolf introduce spatial coherence using Young's two-pinhole interference experiment, an approach similarly emphasized by Mandel and Wolf in *Optical Coherence and Quantum Optics* [134]. Young's experiment serves as a cornerstone for measuring spatial coherence, as it directly evaluates the two-point field correlation function of fields. This measurement is critical in optics, both theoretically and practically. The Young interferometer remains the standard device for this purpose, enabling direct determination of the correlation function's modulus and phase through the visibility and position of the resulting interference fringes. Over the years, several methods have been developed, building on Young's approach to refine and expand its applicability [136-142]. Among these, we highlight a technique that leverages Young's principle and incorporates a DMD for enhanced precision and flexibility [141]. The DMD serves as a programmable aperture array, where micromirrors can be tilted to reflect light into or out of the optical path, effectively creating dynamic pinhole configurations. The DMD can simulate various aperture pairs by controlling which micromirrors are active, allowing coherence measurements at multiple spatial separations.

For a quasi-monochromatic field, the spatial correlations between two points x_1 and x_2 are described by the mutual intensity, $J(x_1\,, x_2)$. This can be expressed as a sum of incoherent coherent modes $U_m(x)$ as

$$J(x_1\,, x_2) = \sum_m I_m U_m^*(x_1)\, U_m(x_2), \tag{1.37}$$

where $U_m(x)$ represents the coherent modes and I_m are their respective weights.

The complex degree of coherence is defined as

$$\mu(x_1, x_2) = \frac{J(x_1, x_2)}{\sqrt{I(x_1)I(x_2)}} = |\mu(x_1, x_2)| exp[i\phi(x_1, x_2)], \quad (1.38)$$

where $|\mu(x_1, x_2)|$ and $\phi(x_1, x_2)$ represent the magnitude and phase of the degree of coherence, respectively.

In Young's experiment, two pinholes are placed at coordinates x_1 and x_2. The intensity distribution on the observation screen, under paraxial conditions, is given by

$$I(x') = I_1(x') + I_2(x') + 2I_1(x')I_2(x')|\mu(x_1, x_2)| cos\left[\phi(x_1, x_2) + \frac{4\pi a}{\lambda_0 d} x'\right], \quad (1.39)$$

where,

- $2a$ is the separation between the pinholes,
- d is the distance to the observation screen,
- λ_0 is the wavelength,
- $I_p(x')$ is the intensity contribution when only pinhole p is open,
- x' is the normalized coordinate relative to the center of the pinhole pair.

The complex degree of coherence can be evaluated by first measuring the intensities $I(x')$, $I_1(x')$, and $I_2(x')$, and then calculating:

$$C(x') = \frac{I(x') - I_1(x') - I_2(x')}{2\sqrt{I_1(x')I_2(x')}} = |\mu(x_1, x_2)| cos\left[\phi(x_1, x_2) + \frac{4\pi a}{\lambda_0 d} x'\right], \quad (1.40)$$

From this sinusoidal curve, the amplitude $|\mu(x_1, x_2)|$ and phase $\phi(x_1, x_2)$ can be extracted.

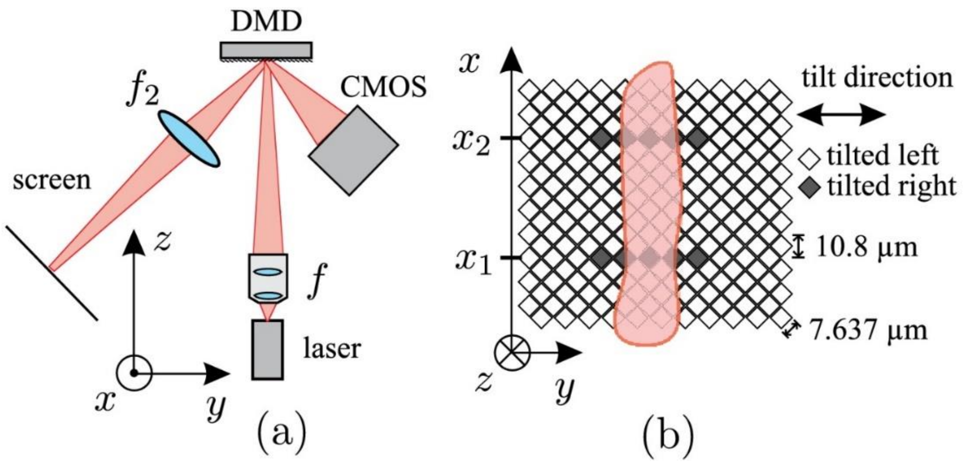

Fig. 1.16 (a) Measurement system. (b) Arrangement of the micromirrors, Young's slits, and the laser spot [141].

Fig. 1.16 (a) illustrates the experimental setup incorporating a DMD chip to create Young's double-pinhole configuration dynamically. The DMD consists of a micromirror array arranged in a diamond orientation, as shown in Fig. 1.16 (b). The DMD acts as a programmable aperture, where mirrors can be tilted to either reflect light toward the detector or deflect it away. A multimode laser diode illuminates the DMD plane through a 10x microscope objective. On the DMD, the pinholes are created as lines of tilted micromirrors that direct light toward a CMOS camera. Bright and dark pixels are controlled by tilting the micromirrors by $+12^{\circ}$ and -12°, respectively. The CMOS camera records the interference pattern created by the selected pinholes. A second lens projects the DMD plane onto a screen for alignment, using markers drawn on the DMD for reference. This configuration allows for precise, programmable aperture control, enabling flexible coherence measurements with high spatial resolution. A detailed discussion of this experiment is available in Ref. 141.

1.5.5.2 Wavefront folding interferometer

The wavefront folding interferometer (WFI) is a versatile tool for measuring spatial coherence by analyzing the two-point correlation of the light field. This method uses the principle of wavefront division, where parts of the wavefront are folded and recombined using an optical element, such as a beam splitter, wedge prism, or reflective surface, to create interference patterns that carry coherence information [143]. Early implementations utilized two-dimensional folding WFIs, where the plane mirror, as shown in Fig. 1.17, was replaced by a retroreflector to fold the incoming wavefront along the x and y directions. In these setups, the retroreflectors were typically aligned such that their corners coincided with the optical axis ($s = 0$ in Fig. 1.17). This configuration provides the coherence measurement to pairs of axially symmetric points.

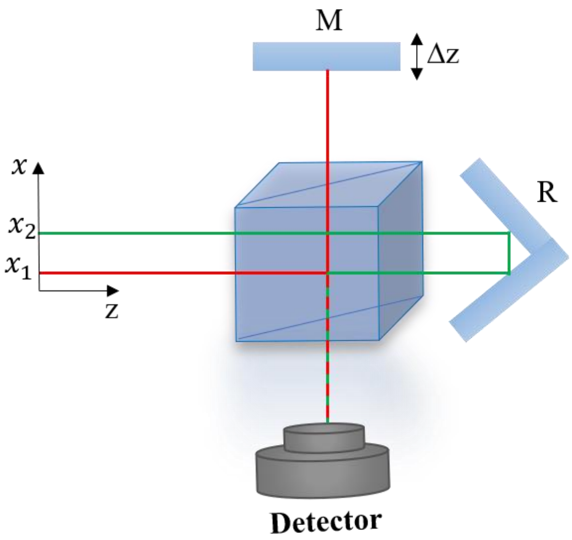

Fig. 1.17 Schematic of a 1D folding WFI [144].

The system in Fig. 1.17 introduces a one-dimensional (1D) folding WFI with arbitrary shear s. This design enables the measurement of spatial coherence between any two points x_1 and x_2, providing greater flexibility and a broader range of coherence information. In the WFI, the input field is split into two arms: arm 1 uses a retroreflector R (horizontal path), and arm 2 uses a plane mirror M (vertical path), as shown in Fig. 1.17. Rays originating from a point x_1 in the input, the plane overlap with rays from a corresponding point $x_2 = -x_1 + 2s$ at the output plane, creating interference. An array detector captures these interference patterns, enabling parallel measurement of coherence between x_1 and x_2.

By tuning the shear s, interference between arbitrary points x_1 and x_2 can be analyzed. A longitudinal shift Δz adjusts the optical path difference for practical control. The spectral interference pattern is given by [144]

$$S(X;\omega) = \frac{1}{4}[S_0(x;\omega) + S_0(2s - x;\omega)] + \frac{1}{2}\sqrt{S_0(x;\omega)S_0(2s - x;\omega)}|\mu_0(x, 2s - x;\omega)|cos[\alpha_0(x, 2s - x;\omega) + \Delta\phi(\omega)], \tag{1.41}$$

where μ_0 is the complex degree of coherence and $\Delta\phi(\omega) = 2(\omega/c)\Delta z$.

Fringe visibility determines the coherence magnitude

$$V(X;\omega) = \frac{2\sqrt{S_0(x;\omega)S_0(2s-x;\omega)}}{S_0(x;\omega)+S_0(2s-x;\omega)}|\mu_0(x, 2s - x;\omega)|, \tag{1.42}$$

while fringe positions reveal the coherence phase $\alpha_0(x, 2s - x;\omega)$.

Therefore, WFI has been a foundational tool for spatial coherence measurement for over half a century. It offers a practical and efficient approach by combining a straightforward setup with a precise analysis of coherence properties. Over the years, various techniques and advancements have been developed based on the WFI to enhance its capabilities further [143-148].

1.5.5.3 Reversed-wavefront interferometer

The reversed-wavefront interferometer (RWI) is a modified version of the classical Young's interferometer, designed to enhance its versatility and simplify coherence measurements, as depicted in Fig. 1.18. This setup uses a beam-splitter (BS) cube to generate two replicas of the incoming wavefront, where one replica is flipped due to reflection within the BS. These reversed, and non-reversed wavefronts propagate along parallel paths and are directed toward a mask containing two pinholes. In this configuration, each pinhole samples a point from one of the wavefront replicas, enabling the measurement of spatial coherence without needing to vary the positions of the pinholes. The RWI keeps the distance between the pinholes fixed and relies on the lateral movement of the BS to adjust the separation between the replicas, allowing coherence measurements across different regions of the wavefront [149].

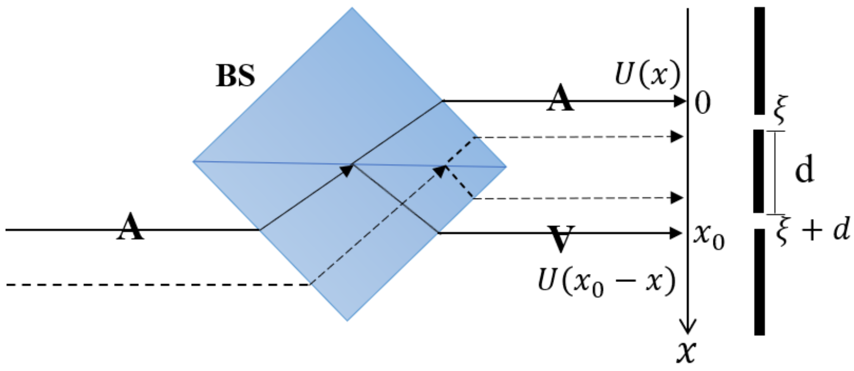

Fig. 1.18 Schematic of a 1D RWI.

If the incident field distribution is $U(x)$, the field at the transverse plane after the BS is

$$U_{BS}(x) = U(x) + U(x_0 - x), \tag{1.43}$$

where x_0 represents the distance between the two wavefront replicas. The pinholes in the Young mask sample fields at positions $x_1 = x_0 - d - \xi$ (from the flipped wavefront) and $x_2 = \xi$ (from the original wavefront), where d is the fixed distance between the pinholes.

The intensity $I(x_f)$ at the far-field focal plane of a lens with focal length f is given by

$$I(x_f) = I_1 + I_2 + 2\sqrt{I_1 I_2}|\gamma_{12}|cos\left(\frac{2\pi d}{\lambda f}x_f + \phi_{12}\right), \tag{1.44}$$

where,

- x_f: transverse coordinate at the focal plane,
- λ: wavelength of the light,

- $I_1 = |\langle U(x_0 - d - \xi\ )\rangle|^2$, $I_2 = |\langle U(\xi\ )\rangle|^2$: intensities when pinholes 1 and 2 are open,
- γ_{12} is the spectral degree of coherence
- ϕ_{12}: phase difference between the fields at x_1 and x_2.

Coherence can be measured for various pairs of points by varying the lateral position of the BS or adjusting the average position of the pinholes.

1.5.5.4 Multiple apertures

The spatial coherence of a light field is traditionally measured using a double-aperture interferometer, as demonstrated in the classic Young's double-slit experiment. By systematically varying the spacing and orientation of the apertures and shifting the double-aperture mask, one can evaluate the spatial coherence across the entire plane of the light field. However, this method requires numerous iterations, as each coherence data point necessitates a separate measurement, resulting in a time-consuming process. To address this limitation, a more efficient technique has been proposed. This method involves using an array of apertures to analyze the light field. By illuminating this mask and recording the resulting far-field interferogram with a charge-coupled device (CCD) camera, as shown in Fig. 1.19, the spatial coherence can be determined directly from the Fourier spectrum of the interferogram [150-152]. The Fourier spectrum contains a distribution of peaks whose positions correspond to the separation vectors of aperture pairs, and the heights of these peaks are directly related to the spatial coherence and intensity correlations between the aperture pairs. The phases of these peaks encode the phase information of the spatial coherence. The key advantage of this approach lies in its ability to extract coherence information for multiple point pairs from a single interferogram. By strategically designing the aperture array, it becomes possible to gather data for numerous point pairs along the wavefront simultaneously. For a mask containing N pinholes, up to $(N-1)!$ pairwise measurements can be achieved, enabling the efficient characterization of spatial coherence. Mathematically, the Fourier transform of the interferogram provides information about the degree of coherence $\mu(\boldsymbol{r}_n, \boldsymbol{r}_m)$ between any two points $\boldsymbol{r}_n$ and $\boldsymbol{r}_m$, corresponding to the positions of apertures n and m, respectively. The relative amplitudes of the Fourier spectrum are directly proportional to the intensity correlations between chosen aperture pairs, described by the following relationship

$$\tilde{I}(\boldsymbol{r}) = \Lambda(\boldsymbol{r}) \otimes \left[\sum_{n=1}^{N} I_n \delta(\boldsymbol{r}) + \sum_{n=m+1}^{N} \sum_{m=1}^{N-1} \sqrt{I_n I_m} \{\mu(\boldsymbol{r}_n, \boldsymbol{r}_m)\delta(\boldsymbol{r} - \boldsymbol{d}_{nm}) + \mu^*(\boldsymbol{r}_n, \boldsymbol{r}_m)\delta(\boldsymbol{r} + \boldsymbol{d}_{nm})\}\right], \tag{1.45}$$

where,

- $\tilde{I}(\boldsymbol{r})$ is the Fourier transform of the interference pattern in the observation plane.
- $\otimes$ denotes convolution.
- $\Lambda(\boldsymbol{r})$ is the autocorrelation function of a single pinhole (assuming all pinholes are identical).
- I_n and I_m are the intensities contributed by the apertures at positions $\boldsymbol{r}_n$ and $\boldsymbol{r}_m$, respectively.
- $\boldsymbol{d}_{nm} = \boldsymbol{r}_n - \boldsymbol{r}_m$ is the separation vector between two apertures.

The modulus of the complex DOC can be expressed as

$$\mu(\boldsymbol{r}_n, \boldsymbol{r}_m) = \frac{C_{nm}}{\sqrt{I_n I_m}} \frac{S_0}{|C_0|}, \tag{1.46}$$

where,

- $S_0 = \sum_{n=m} I_m$ is the total intensity through the mask.

- C_0 is the amplitude of the zeroth-order peak in the Fourier spectrum.

- C_{nm} is the amplitude of the peak corresponding to the separation vector $\boldsymbol{d}_{nm}$.

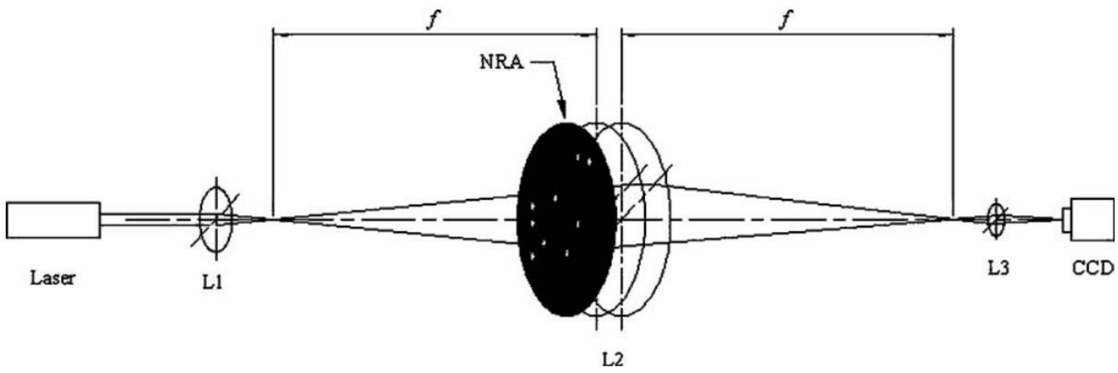

Fig. 1.19 Measurement of spatial coherence using nonredundant array (NRA) of apertures, L: Lens, CCD: Camera [151].

This method leverages the Fourier transform's ability to link the interference pattern to the correlations within the light field, facilitating efficient spatial coherence measurement. The convolution accounts for the autocorrelation of individual apertures, while the peak amplitudes and phases provide insights into the coherence properties of the light field. This approach is particularly effective for complex light sources, enabling simultaneous analysis of multiple coherence data points. This approach is particularly effective for studying complex or exotic light sources, such as x-ray free-electron lasers (FELs) and synchrotron radiation. Recent studies have even applied this technique to characterize x-ray beams generated through high harmonic generation, showcasing its versatility and precision [153].

1.5.5.5 Sagnac-type interferometers

A novel method for measuring the Spatial Coherence Function (SCF) integrates interferometric principles with advanced optical setups. The SCF, representing field-field correlations, can be extracted using either wavefront sampling or wavefront shearing approaches. Traditional techniques like Young's experiment and its derivatives (e.g., pinhole arrays and slit-based methods) offer improved performance but face challenges like light throughput and experimental complexity. There are various methods to introduce shear in interferometric setups. One approach, as described in Ref. [154], uses a rotating glass slab to displace counterpropagating beams in opposite directions laterally, enabling the recording of interference patterns for different shear configurations. Shear interferometers that rely on repositioning refractive elements, such as lenses or glass slabs [155, 156], and employing the translation of reflective elements, are also developed [157, 158]. Fig. 1.20 shows a lateral shearing Sagnac Interferometer [157]. The core idea involves dividing the input optical beam into two identical parts, separated spatially by a shear distance s. These two sheared beams are then interfered to produce an interferogram, described by

$$I^{\delta}(x,s) = \langle |U(x+s/2) + U(x-s/2)|^2 \rangle,$$

$$= \langle |U(x+s/2)|^2 \rangle + \langle |U(x-s/2)|^2 \rangle + Re[2\langle U(x+s/2)U^*(x-s/2)\rangle exp(i\delta)], \tag{1.47}$$

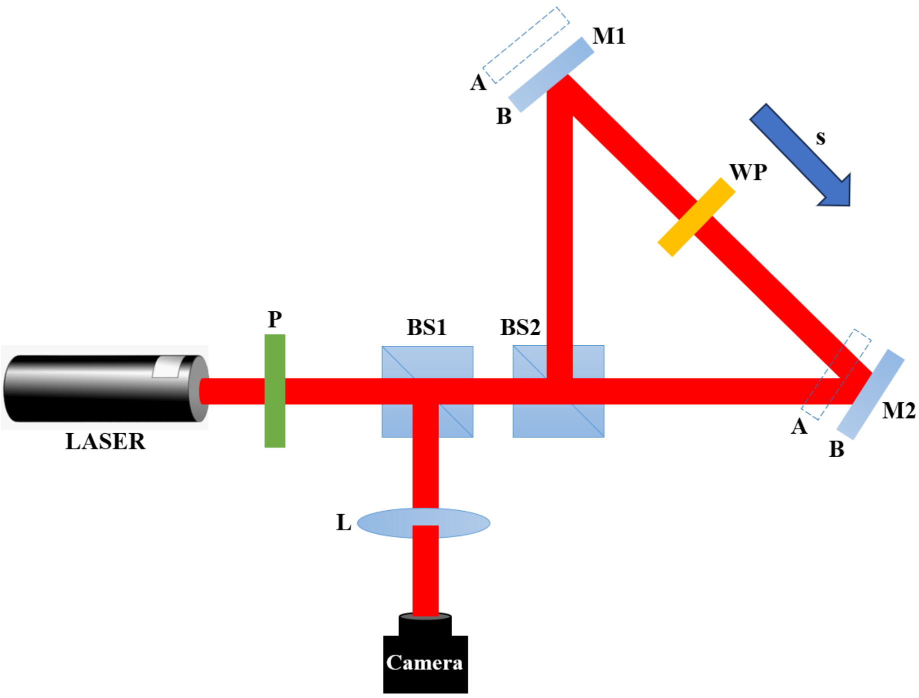

Fig. 1.20 Measurement of spatial coherence using Sagnac shearing interferometer.

where δ represents the phase shift between the two beams, and Re denotes the real part. The first two terms correspond to the intensities of the individual beams, while the third term captures the interference between the two, reflecting the coherence properties of the light field.

In the setup Fig. 1.20, light from the laser is linearly polarized using a polarizing cube (P) and passes through a nominal 50/50 non-polarizing beam splitter (BS1) before entering the Sagnac interferometer via a second beam splitter (BS2). Inside the interferometer, the light splits into two beams traveling in opposite directions (clockwise and counterclockwise), which undergo equal but opposite lateral shears before recombining at BS2 for interference. The interferogram is partially reflected by BS1 and recorded using a CCD camera. Lateral shearing is achieved through free-space propagation by translating a pair of mirrors (M1 and M2) along the propagation axis, ensuring no astigmatism is introduced—an essential consideration for a high numerical aperture system. The phase shift δ between the sheared beams is introduced via wave plates (WP), where polarization directions of the counter-propagating beams are aligned with either the fast or slow axes of the wave plate to induce a relative phase delay. By selecting appropriate phase shifts (0, $\pi/2$, π, $3\pi/2$), four distinct interferograms are recorded. Pixel-by-pixel computations on these patterns are performed post-acquisition to extract both the real and imaginary components of the spatial coherence function (SCF), offering precise measurement of coherence properties.

Other than these there are several other methods developed over years for the measurement of spatial coherence based on Mach-Zehnder interferometers [159, 160], grating interferometers [161, 162], non- parallel double slits [163], shadowing obstacles [164], nanoscatteres [165], discontinuous phase mask [166], coherence holography [167-169], self-referencing holography [170], etc.

1.5.6 Unified theory of coherence and polarization

We have examined the coherence properties of light beams modeled as scalar optical fields, where the polarization remains constant across a given section. The investigations thus far have primarily relied on scalar theory. However, to fully understand another important property of light, polarization, we must consider the vector nature of the light. Polarization provides a deeper insight into how the field behaves in three dimensions involving the orientation and magnitude of the electric field vector at any given point. The theory of polarization has evolved significantly over time, beginning in 1852 when G.G. Stokes introduced the Stokes parameters, which remain fundamental in describing the polarization state of light [134, 171]. Later, in 1930, Wiener expanded on this by establishing a relationship between the electric field correlation and the polarization properties of light using the matrix method [172]. A comprehensive historical account of polarization theory development can be found in Ref. [173]. In 1941, R.C. Jones further contributed by developing the Jones calculus and the associated Jones matrix, providing a robust framework for analyzing the polarization states of light [174]. This was followed by H. Mueller's work on the generalized polarization matrix, which expanded the scope of analysis. S. Pancharatnam made a groundbreaking contribution by generalizing the interference theory and introducing the concept of a geometrical phase associated with transitions between different polarization states [175, 176]. M.V. Berry later extended this idea to the quantum realm in his study of quantum cyclic evolution, leading to the discovery of the Berry phase, a key concept in quantum mechanics [177].

While scalar theory explains many aspects of optical coherence, polarization requires a more comprehensive, vectorial description of the electromagnetic field. Thus, the pioneering work of Wolf unified the concept of coherence and polarization into a comprehensive theory, demonstrating their intrinsic connection. Coherence describes the correlation between orthogonal electric field components at two spatial points, while polarization focuses on the correlation at a single point. The degree of coherence or correlation between fluctuations in a light field is fundamentally characterized using various correlation functions in space-time and space-frequency domains. These functions enable a detailed understanding of coherence properties, facilitating the description and prediction of several phenomena related to optical fields. Extending the coherence matrix, the two-point (spatial) generalization leads to the formulation of two distinct 2 × 2 matrices: the beam coherence-polarization (BCP) matrix in the space-time domain and the cross-spectral density (CSD) matrix in the space-frequency domain [178-180]. These matrices provide a unified framework to simultaneously analyze light's coherence and polarization characteristics in their respective domains, contributing significantly to the field of optical coherence theory.

Consider a stochastic electromagnetic beam propagating in the z-direction with two points P_1 and P_2 having position vectors $\boldsymbol{r}_1$ and $\boldsymbol{r}_2$, respectively, within the beam's cross-section. Observing the beam at a point P in the observation plane with position vector $\boldsymbol{r}$, we can analyze the coherence and polarization properties of the beam in the space-time domain through a 2 × 2 BCP matrix, defined as [2, 134]

$$\mathbf{J}(\boldsymbol{r}_1, \boldsymbol{r}_2, t) = \begin{bmatrix} \langle U_x^*(\boldsymbol{r}_1, t) U_x(\boldsymbol{r}_2, t) \rangle & \langle U_x^*(\boldsymbol{r}_1, t) U_y(\boldsymbol{r}_2, t) \rangle \\ \langle U_y^*(\boldsymbol{r}_1, t) U_x(\boldsymbol{r}_2, t) \rangle & \langle U_y^*(\boldsymbol{r}_1, t) U_y(\boldsymbol{r}_2, t) \rangle \end{bmatrix}, \tag{1.48}$$

Here, $*$ denotes the complex conjugate, and $\langle \cdot \rangle$ represents the ensemble average. Unlike the classical coherence matrix with constant parameters, the BCP matrix elements depend on the spatial positions $\boldsymbol{r}_1$ and $\boldsymbol{r}_2$. In cases where spatial dependence vanishes, the BCP matrix reduces to the coherence matrix.

The complex degree of cross-coherence is defined as a normalized measure of the cross-correlation function

$$\gamma(\boldsymbol{r}_1, \boldsymbol{r}_2) = \frac{\mathrm{Tr}[\mathbf{J}(\boldsymbol{r}_1, \boldsymbol{r}_2)]}{\sqrt{\mathrm{Tr}[\mathbf{J}(\boldsymbol{r}_1, \boldsymbol{r}_1)]\mathrm{Tr}[\mathbf{J}(\boldsymbol{r}_2, \boldsymbol{r}_2)]}}, \tag{1.49}$$

In the space-frequency domain, the second-order coherence properties are similarly characterized by the electric CSD matrix, defined as [2, 134]

$$\mathbf{W}(\boldsymbol{r}_1, \boldsymbol{r}_2, \omega) = \begin{bmatrix} \langle U_x^*(\boldsymbol{r}_1, \omega) U_x(\boldsymbol{r}_2, \omega) \rangle & \langle U_x^*(\boldsymbol{r}_1, \omega) U_y(\boldsymbol{r}_2, \omega) \rangle \\ \langle U_y^*(\boldsymbol{r}_1, \omega) U_x(\boldsymbol{r}_2, \omega) \rangle & \langle U_y^*(\boldsymbol{r}_1, \omega) U_y(\boldsymbol{r}_2, \omega) \rangle \end{bmatrix}, \tag{1.50}$$

The spectral degree of coherence is

$$\mu(\boldsymbol{r}_1, \boldsymbol{r}_2, \omega) = \frac{\mathrm{Tr}[\mathbf{W}(\boldsymbol{r}_1, \boldsymbol{r}_2, \omega)]}{\sqrt{\mathrm{Tr}[\mathbf{W}(\boldsymbol{r}_1, \boldsymbol{r}_1, \omega)]\mathrm{Tr}[\mathbf{W}(\boldsymbol{r}_1, \boldsymbol{r}_1, \omega)]}}, \tag{1.51}$$

with $0 \le |\mu(\boldsymbol{r}_1, \boldsymbol{r}_2, \omega)| \le 1$, representing incoherence ($|\mu| = 0$), complete coherence ($|\mu| = 1$), or partial coherence ($0 < |\mu| < 1$).

BCP and CSD matrices unify coherence and polarization analysis despite being defined in different domains. Under quasi-monochromatic or narrowband conditions, results from both domains align closely, showcasing their equivalence in describing electromagnetic beam properties [181, 182].

Also, the framework of Stokes parameters, traditionally used to describe polarization, can be extended by generalizing the conventional one-point Stokes parameters to two-point quantities. This generalization integrates the spatial coherence properties with the polarization characteristics of light beams, offering a more comprehensive description of their behavior [183]. An important distinction is that, unlike the usual Stokes parameters, the generalized Stokes parameters (GSPs) adhere to propagation laws in free space and linear media [184]. This feature allows for analyzing changes in one-point Stokes parameters during beam propagation using the two-point Stokes parameters. In the space-frequency domain, the GSPs are defined as

$$S_0(\boldsymbol{r}_1, \boldsymbol{r}_2, \omega) = \langle U_x^*(\boldsymbol{r}_1, \omega) U_x(\boldsymbol{r}_2, \omega)\rangle + \langle U_y^*(\boldsymbol{r}_1, \omega) U_y(\boldsymbol{r}_2, \omega)\rangle, \tag{1.52}$$

$$S_1(\boldsymbol{r}_1, \boldsymbol{r}_2, \omega) = \langle U_x^*(\boldsymbol{r}_1, \omega) U_x(\boldsymbol{r}_2, \omega)\rangle - \langle U_y^*(\boldsymbol{r}_1, \omega) U_y(\boldsymbol{r}_2, \omega)\rangle, \tag{1.53}$$

$$S_2(\boldsymbol{r}_1, \boldsymbol{r}_2, \omega) = \langle U_x^*(\boldsymbol{r}_1, \omega) U_y(\boldsymbol{r}_2, \omega)\rangle + \langle U_y^*(\boldsymbol{r}_1, \omega) U_x(\boldsymbol{r}_2, \omega)\rangle, \tag{1.54}$$

$$S_3(\boldsymbol{r}_1, \boldsymbol{r}_2, \omega) = i\left[\langle U_y^*(\boldsymbol{r}_1, \omega) U_x(\boldsymbol{r}_2, \omega)\rangle - \langle U_x^*(\boldsymbol{r}_1, \omega) U_y(\boldsymbol{r}_2, \omega)\rangle\right], \tag{1.55}$$

These parameters can be equivalently expressed using the elements of the CSD matrix

$$S_0(\boldsymbol{r}_1, \boldsymbol{r}_2, \omega) = W_{\boldsymbol{xx}}(\boldsymbol{r}_1, \boldsymbol{r}_2, \omega) + W_{\boldsymbol{yy}}(\boldsymbol{r}_1, \boldsymbol{r}_2, \omega), \tag{1.56}$$

$$S_1(\boldsymbol{r}_1, \boldsymbol{r}_2, \omega) = W_{\boldsymbol{xx}}(\boldsymbol{r}_1, \boldsymbol{r}_2, \omega) - W_{\boldsymbol{yy}}(\boldsymbol{r}_1, \boldsymbol{r}_2, \omega), \tag{1.57}$$

$$S_2(\boldsymbol{r}_1, \boldsymbol{r}_2, \omega) = W_{\boldsymbol{xy}}(\boldsymbol{r}_1, \boldsymbol{r}_2, \omega) + W_{\boldsymbol{yx}}(\boldsymbol{r}_1, \boldsymbol{r}_2, \omega), \tag{1.58}$$

$$S_3(\boldsymbol{r}_1, \boldsymbol{r}_2, \omega) = i\left[W_{\boldsymbol{yx}}(\boldsymbol{r}_1, \boldsymbol{r}_2, \omega) - W_{\boldsymbol{xy}}(\boldsymbol{r}_1, \boldsymbol{r}_2, \omega)\right], \tag{1.59}$$

where $W_{\boldsymbol{sq}}(\boldsymbol{r}_1, \boldsymbol{r}_2, \omega)(s, q = x, y)$ are elements of the electric CSD matrix. Similarly, GSPs can be defined using the BCP matrix in the space-time domain. These generalized parameters are linear combinations of the CSD matrix elements, making them versatile tools for characterizing coherence and polarization. Thus, GSPs offer a robust alternative to the CSD matrix for studying the interplay of coherence and polarization in random electromagnetic beams, emphasizing their shared foundation and utility in optical studies [185-187].

1.5.7 Measurement of vectorial spatial coherence

The measurement of vectorial coherence has become a pivotal aspect of understanding the behavior of partially coherent vector light, which extends the properties of scalar random light to the vector domain. Such light demonstrates complex polarization and coherence characteristics, particularly during propagation, interference, and light-matter interactions. Several methods have been developed for measuring vectorial spatial coherence, primarily focusing on the BCP matrix and the CSD matrix. These approaches have significantly advanced our understanding of vector fields' coherence and polarization characteristics. Below is an overview of prominent techniques.

1.5.7.1 Young's interferometer

After the advent of the unified theory of coherence and polarization, the initial method for measuring the correlation matrix was based on Young's double-slit interference experiment. Wolf proposed that the four elements of the electric CSD matrix could be determined by analyzing the spectral changes in a Young's experiment with polarizers and a rotator positioned in front of the pinholes as represented in Fig. 1.21 [188].

For a random electromagnetic beam propagating in the *z*-direction, its second-order coherence properties are described by the CSD matrix

$$\mathbf{W}(\boldsymbol{r}_1, \boldsymbol{r}_2, \omega) = \begin{bmatrix} W_{xx}(\boldsymbol{r}_1, \boldsymbol{r}_2, \omega) & W_{xy}(\boldsymbol{r}_1, \boldsymbol{r}_2, \omega) \\ W_{yx}(\boldsymbol{r}_1, \boldsymbol{r}_2, \omega) & W_{yy}(\boldsymbol{r}_1, \boldsymbol{r}_2, \omega) \end{bmatrix}, \tag{1.60}$$

where $W_{sq}(\boldsymbol{r}_1, \boldsymbol{r}_2, \omega) = \langle U_s^*(\boldsymbol{r}_1, \omega) U_q(\boldsymbol{r}_2, \omega) \rangle$, $s, q = x, y$, ω is the frequency and $\langle \cdot \rangle$ denotes the ensemble average.

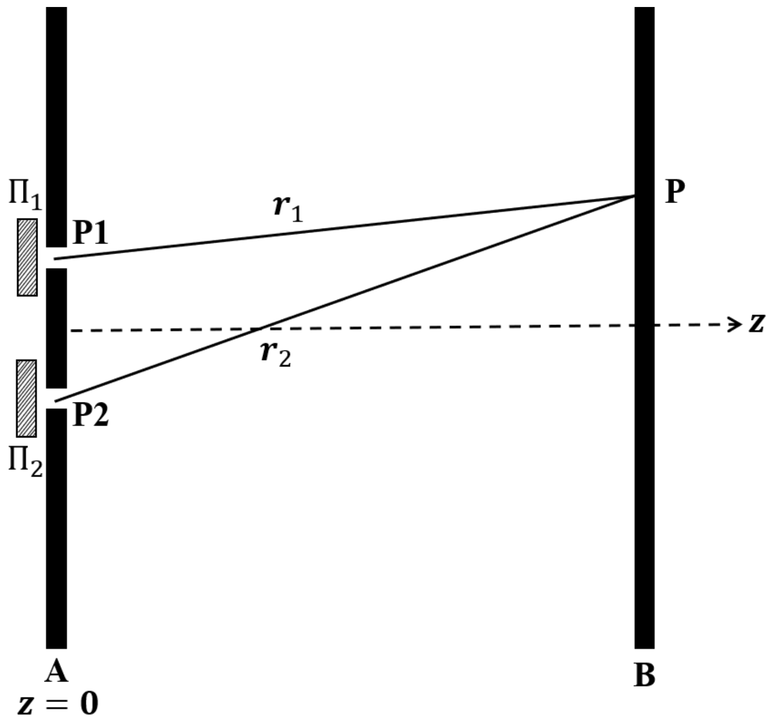

Fig. 1.21 Schematic diagram of the Young's interference experiment for the measurement of CSD matrix [188].

Consider an opaque screen placed in the $z = 0$ plane, with two narrow slits symmetrically positioned about a line perpendicular to the plane as shown in Fig. 1.21. Denoting two arbitrary points in the slits as $P1$ and $P2$, their respective position vectors are $\boldsymbol{r}_1$ and $\boldsymbol{r}_2$. The spectral degree of coherence of the electric field at these points is expressed as [188]

$$\mu(\boldsymbol{r}_1, \boldsymbol{r}_2, \omega) = \frac{\mathrm{Tr}[\mathbf{W}(\boldsymbol{r}_1, \boldsymbol{r}_2, \omega)]}{\sqrt{\mathrm{Tr}[\mathbf{W}(\boldsymbol{r}_1, \boldsymbol{r}_1, \omega)]\mathrm{Tr}[\mathbf{W}(\boldsymbol{r}_1, \boldsymbol{r}_1, \omega)]}}, \tag{1.61}$$

This equation can be reformulated as

$$\mathrm{Tr}[\mathbf{W}(\boldsymbol{r}_1, \boldsymbol{r}_2, \omega)] = \sqrt{S(\boldsymbol{r}_1, \omega)}\sqrt{S(\boldsymbol{r}_2, \omega)}\mu(\boldsymbol{r}_1, \boldsymbol{r}_2, \omega), \tag{1.62}$$

Therefore, the trace of the CSD matrix, $\mathbf{W}(\boldsymbol{r}_1, \boldsymbol{r}_2, \omega)$, can be determined by combining the spectral measurements $S(\boldsymbol{r}_1, \omega)$ and $S(\boldsymbol{r}_2, \omega)$ at points $\boldsymbol{r}_1$ and $\boldsymbol{r}_2$ in the plane $z = 0$ with the spectral degree of coherence, $\mu(\boldsymbol{r}_1, \boldsymbol{r}_2, \omega)$, evaluated between these points. The components of the CSD matrix $\mathbf{W}(\boldsymbol{r}_1, \boldsymbol{r}_2, \omega)$ can be determined as

$$\mathbf{W}(\boldsymbol{r}_1, \boldsymbol{r}_2, \omega) = W_{sq}(\boldsymbol{r}_1, \boldsymbol{r}_2, \omega) = \sqrt{S_s(\boldsymbol{r}_1, \omega)}\sqrt{S_q(\boldsymbol{r}_2, \omega)}\mu_{sq}(\boldsymbol{r}_1, \boldsymbol{r}_2, \omega), \quad s, q = x, y \tag{1.63}$$

Here, $S_s(\boldsymbol{r}_1, \omega)$ and $S_q(\boldsymbol{r}_2, \omega)$ represent the spectral densities at the respective points, and $\mu_{sq}(\boldsymbol{r}_1, \boldsymbol{r}_2, \omega)$ denotes the spectral degree of coherence.

To retrieve different components of the CSD matrix, polarizers Π1 and Π2 are positioned in front of the two slits and adjusted appropriately. For instance, if the polarizers are oriented to allow only the x-component of the incident beam to pass, the component $W_{xx}(\boldsymbol{r}_1, \boldsymbol{r}_2, \omega)$ of the CSD matrix can be measured. Similarly, by configuring the polarizers to transmit only the y-component of the beam, the $W_{yy}(\boldsymbol{r}_1, \boldsymbol{r}_2, \omega)$ element can be retrieved. This selective manipulation enables the systematic reconstruction of the full CSD matrix by isolating its individual polarization-dependent components.

A close connection between degree of coherence and degree of polarization of the vector light has been discussed using different approach [189-192]. Later, Setälä et al. demonstrated in Young's two-pinhole experiment that the degree of coherence could be quantitatively linked to the contrast in the modulation of the four Stokes parameters. This includes the visibility of intensity fringes and the modulation strength of the three polarization-related Stokes parameters [193]. The experimental validation of Young's approach for measuring the CSD matrix and evaluating GSPs has been confirmed through various studies, as referenced in [194], [195], [196], and [197]. These works provide detailed insights into the methodology and its effectiveness in characterizing coherence and polarization properties.

1.5.7.2 Vectorial coherence holography

Coherence Holography (CH) offers a novel approach for reconstructing objects using the spatial coherence function of light, diverging from conventional holography, which relies on reconstructing the optical field [168, 169]. This method, when extended to the vectorial regime, forms Vectorial Coherence Holography (VCH), enabling the synthesis and manipulation of vectorial fields characterized by specific elements of the coherence-polarization matrix [198]. The VCH framework is grounded in the generalized van Cittert-Zernike theorem for electromagnetic waves, which serves as the foundation for the theoretical and experimental implementation of this technique [199-201]. In this method, two holograms are employed, each corresponding to one orthogonal polarization component of the vector field. For example, the U_x and U_y components of an object are independently encoded into two Fourier-transform holograms $H_x(\mathbf{v})$ and $H_y(\mathbf{v})$, respectively. These holograms are then illuminated with spatially incoherent vector light, maintaining the same polarization state as during recording. The reconstruction process involves determining the coherence-polarization properties of the field. The complex amplitudes of the orthogonal polarization components behind the hologram are expressed as

$$U_s(\mathbf{v}) = H_s(\mathbf{v}) exp[i\phi_s(\mathbf{v})], \qquad s = x, y \tag{1.64}$$

where $\phi_s(\mathbf{v})$ is a random phase introduced to destroy spatial coherence.

The optical Fourier transform lens projects these fields onto an observation plane, and the reconstructed field is given by

$$U_s(\mathbf{r}) = \int U_s(\mathbf{v}) exp\left(-i\frac{2\pi}{\lambda f}\mathbf{r}.\mathbf{v}\right) d\mathbf{v}, \tag{1.65}$$

The second-order correlation properties of the electromagnetic field are described by the coherence-polarization matrix

$$W_{sq}(\boldsymbol{r}_1,\boldsymbol{r}_2) = \langle U_s^*(\boldsymbol{r}_1)U_q(\boldsymbol{r}_2)\rangle, \qquad s,q = x,y$$

$$= \iint \langle U_s^*(\mathbf{v}_1)U_q(\mathbf{v}_2)\rangle\, exp\left[-i\frac{2\pi}{\lambda f}(\boldsymbol{r}_2.\mathbf{v}_2 - \boldsymbol{r}_1.\mathbf{v}_1)\right] d\mathbf{v}_2 d\mathbf{v}_1$$

$$= \iint H_s^*(\mathbf{v}_1)H_q(\mathbf{v}_2)\langle exp\left[i\phi_s(\mathbf{v}_2) - i\phi_q(\mathbf{v}_1)\right]\rangle exp\left[-i\frac{2\pi}{\lambda f}(\boldsymbol{r}_2.\mathbf{v}_2 - \boldsymbol{r}_1.\mathbf{v}_1)\right] d\mathbf{v}_2 d\mathbf{v}_1, \quad (1.66)$$

When the orthogonal polarization components pass through the same random phase screen, modeled as a delta-correlated phase screen, the phase term simplifies due to the correlation properties as

$$\langle exp\left[i\phi_s(\mathbf{v}_2) - i\phi_q(\mathbf{v}_1)\right]\rangle = \delta(\mathbf{v}_2 - \mathbf{v}_1), \quad (1.67)$$

Using this assumption, the coherence-polarization matrix simplifies into the vectorial van Cittert-Zernike theorem

$$W_{sq}(\Delta\boldsymbol{r}) = \int H_s^*(\mathbf{v})H_q(\mathbf{v})exp\left(-i\frac{2\pi}{\lambda f}\Delta\boldsymbol{r}.\mathbf{v}\right)d\mathbf{v}, \quad (1.68)$$

where $\Delta\boldsymbol{r} = \boldsymbol{r}_2 - \boldsymbol{r}_1$, where $H_s(\mathbf{v})$ and $H_q(\mathbf{v})$ denote the amplitude transmittance of the hologram for polarization components s and q, respectively. The diagonal elements of this matrix $(s = q)$ are real-valued and describe the intensity-related properties of the individual polarization components. In contrast, the off-diagonal elements $(s \neq q)$ may be complex and provide information about the cross-correlation between orthogonal polarization components. A comprehensive discussion of the experimental setup and its underlying principles can be found in Ref. 198.

1.5.7.3 Apertures

Other method for measuring the BCP matrix of paraxial, partially coherent beams utilizes diffraction from small apertures and obstacles, employing only a SLM to implement the obstacle, a lens for performing the optical Fourier transform, and a CCD detector for capturing intensity distributions, as shown in Fig.1.22 [202]. Additionally, polarization selection elements are incorporated to enable the measurement of the full correlation matrix. To achieve this, they leverage the concept of GSPs, defined as

$$S_0(\boldsymbol{r}_1,\boldsymbol{r}_2) = J_{xx}(\boldsymbol{r}_1,\boldsymbol{r}_2) + J_{yy}(\boldsymbol{r}_1,\boldsymbol{r}_2), \tag{1.69}$$

$$S_1(\boldsymbol{r}_1,\boldsymbol{r}_2) = J_{xx}(\boldsymbol{r}_1,\boldsymbol{r}_2) - J_{yy}(\boldsymbol{r}_1,\boldsymbol{r}_2), \tag{1.70}$$

$$S_2(\boldsymbol{r}_1,\boldsymbol{r}_2) = J_{pp}(\boldsymbol{r}_1,\boldsymbol{r}_2) + J_{mm}(\boldsymbol{r}_1,\boldsymbol{r}_2) = J_{xy}(\boldsymbol{r}_1,\boldsymbol{r}_2) + J_{yx}(\boldsymbol{r}_1,\boldsymbol{r}_2), \tag{1.71}$$

$$S_3(\boldsymbol{r}_1,\boldsymbol{r}_2) = J_{rr}(\boldsymbol{r}_1,\boldsymbol{r}_2) + J_{ll}(\boldsymbol{r}_1,\boldsymbol{r}_2) = i\left[J_{yx}(\boldsymbol{r}_1,\boldsymbol{r}_2) - J_{xy}(\boldsymbol{r}_1,\boldsymbol{r}_2)\right], \tag{1.72}$$

where $J_{sq}(\boldsymbol{r}_1,\boldsymbol{r}_2) = \langle U_s^*(\boldsymbol{r}_1)U_q(\boldsymbol{r}_2)\rangle$, $s,q = x,y$ are the components of the BCP matrix and the subscripts p, m refer to axes oriented at +45° and −45 ° to the x-axis, while r, l denote right- and left-handed circular polarizations, respectively.

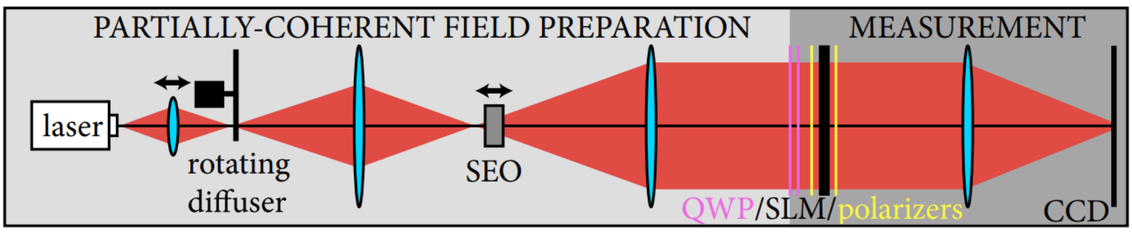

Fig. 1.22 Schematics of the experimental setup based on Young's interferometer [202].

The spatial coherence associated with specific field components is measured by capturing images in a Fourier-conjugate plane, where the optical Fourier transform is performed by a lens in a $2f$-configuration as shown in Fig. 1.22. A field component U_n ($n =$

x, y, p, m, r, l) is selected using waveplates and polarizers, and then passed through a test plane containing a simple aperture mask. To measure the correlation $J_{nn}(\boldsymbol{r}_1, \boldsymbol{r}_2)$, images are captured under four conditions: (i) with a clear mask, (ii) with a small opaque obstacle at the centroid x_0, (iii) with a complementary small aperture at x_0, and (iv) with the SLM completely darkened. Let these measured intensities be $I^n(\boldsymbol{u})$, $I_O^n(\boldsymbol{u}; \boldsymbol{r}_0)$, $I_A^n(\boldsymbol{u}; \boldsymbol{x}_0)$, and $I_D^n(\boldsymbol{u})$, respectively, where $\boldsymbol{u}$ is the coordinate at CCD plane. Under the assumption that the apertures and obstacles are small, the correlation component is approximated as

$$J_{nn}\left(\boldsymbol{r}_0 - \frac{\boldsymbol{r}'}{2}, \boldsymbol{r}_0 + \frac{\boldsymbol{r}'}{2}\right) \propto \iint I^n(\boldsymbol{u}) - I_O^n(\boldsymbol{u}; \boldsymbol{r}_0) + I_A^n(\boldsymbol{u}; \boldsymbol{r}_0) -$$

$$I_D^n(\boldsymbol{u}) exp\left(i \frac{k}{f} \boldsymbol{u}.\boldsymbol{r}'\right) dxdy, \tag{1.73}$$

Here, $I_D^n(\boldsymbol{u})$ is used for background subtraction. This process enables the determination of the GSPs, which are used to reconstruct the BCP matrix.

1.5.7.4 Intensity correlation

Tervo et al. first demonstrated the relation between the intensity correlation of vector fields in space-time and the electromagnetic degree of coherence, emphasizing contributions from all four components of the coherence-polarization matrix for Gaussian statistics [189]. This framework extended the intensity correlation concept to vector fields. Building on this, the classic Hanbury Brown–Twiss (HBT) experiment was adapted to recover field correlations for partially coherent vector fields. However, traditional setups could only extract the modulus of field correlations, lacking phase information. Later, innovations by Singh et al. introduced reference random light to the HBT experiment, enabling phase information recovery through Fourier fringe analysis [203]. Inspired by the principles of speckle holography and intensity correlation, Singh et al. later proposed an innovative method to analyze the statistical properties of synthesized random fields by determining the complex 2 × 2 coherence-polarization matrix elements [204]. This approach provides a robust framework for characterizing the coherence and polarization of optical fields, combining experimental and theoretical insights. Here, we present a concise overview of this methodology.

The statistical properties of fluctuating electromagnetic fields along the *z*-axis in space-time can be described by the BCP matrix $\mathbf{J}(\boldsymbol{r}_1, \boldsymbol{r}_2, t)$, expressed as

$$\mathbf{J}(\boldsymbol{r}_1, \boldsymbol{r}_2, t) = \begin{bmatrix} J_{xx}(\boldsymbol{r}_1, \boldsymbol{r}_2, t) & J_{xy}(\boldsymbol{r}_1, \boldsymbol{r}_2, t) \\ J_{yx}(\boldsymbol{r}_1, \boldsymbol{r}_2, t) & J_{yy}(\boldsymbol{r}_1, \boldsymbol{r}_2, t) \end{bmatrix}, \quad (1.74)$$

where $J_{sq}(\boldsymbol{r}_1, \boldsymbol{r}_2, t) = \langle U_s^*(\boldsymbol{r}_1, t) U_q(\boldsymbol{r}_2, t)\rangle$, $s, q = x, y$, with $U_x(\boldsymbol{r}, t)$ and $U_y(\boldsymbol{r}, t)$ being the orthogonal polarization components of the field. The asterisk (*) denotes the complex conjugate, and angular brackets $\langle\cdot\rangle$ represent ensemble averaging.

The two-point intensity correlation $\Gamma(\boldsymbol{r}_1, \boldsymbol{r}_2, t)$ BCP matrix elements as [189]

$$\Gamma(\boldsymbol{r}_1, \boldsymbol{r}_2, t) = \langle \Delta I(\boldsymbol{r}_1, t) \Delta I(\boldsymbol{r}_2, t)\rangle = \sum_{s,q} \left| J_{sq}(\boldsymbol{r}_1, \boldsymbol{r}_2, t) \right|^2, \quad (1.75)$$

where $\Delta I(\boldsymbol{r}, t) = I(\boldsymbol{r}, t) - \langle I(\boldsymbol{r}, t)\rangle$, and $I(\boldsymbol{r}, t) = |U(\boldsymbol{r}, t)|^2$.

Using a combination of polarizing elements, such as a quarter-wave plate (QWP) and a linear polarizer (LP), the scattered field is manipulated [205]. The resultant field, after passing through these elements, is given by

$$U_{res}(\boldsymbol{r}, t) = (\cos^2\theta + i\sin^2\theta)\left(U_x^R(\boldsymbol{r}, t) + U_x^S(\boldsymbol{r}, t)\right) + [(1 - i)\cos\theta\sin\theta]\left(U_y^R(\boldsymbol{r}, t) + U_y^S(\boldsymbol{r}, t)\right) \quad (1.76)$$

where θ is the QWP orientation angle, and $U^R(\boldsymbol{r}, t)$ and $U^S(\boldsymbol{r}, t)$ denote the reference and synthesized fields, respectively.

The two-point intensity correlation for the resultant field is

$$\Gamma(\boldsymbol{r}_1, \boldsymbol{r}_2, t) = |\langle U^*_{res}(\boldsymbol{r}_1, t) U_{res}(\boldsymbol{r}_2, t)\rangle|^2, \tag{1.77}$$

For specific QWP rotations $\theta = 0^\circ, 22.5^\circ, 45^\circ, 135^\circ$, the intensity correlations yield holograms that encode the BCP matrix elements. These can be extracted using Fourier fringe analysis, translating the spectral components to obtain $\mathbf{J}(\boldsymbol{r}_1, \boldsymbol{r}_2, t)$ as the inverse Fourier transform of the centrally shifted spectra.

The experimental setup designed to synthesize and analyze the statistical properties of fluctuating electromagnetic fields comprises two main components: the synthesis and analysis blocks. The synthesis block, enclosed within dotted lines in Fig. 1.23, uses an inner interferometer to generate the desired random field. The analysis block applies speckle interferometry and two-point intensity correlation through spatial averaging. To measure the BCP matrix elements, a QWP and a LP are utilized. A detailed description of the experiment can be found in Ref. [204].

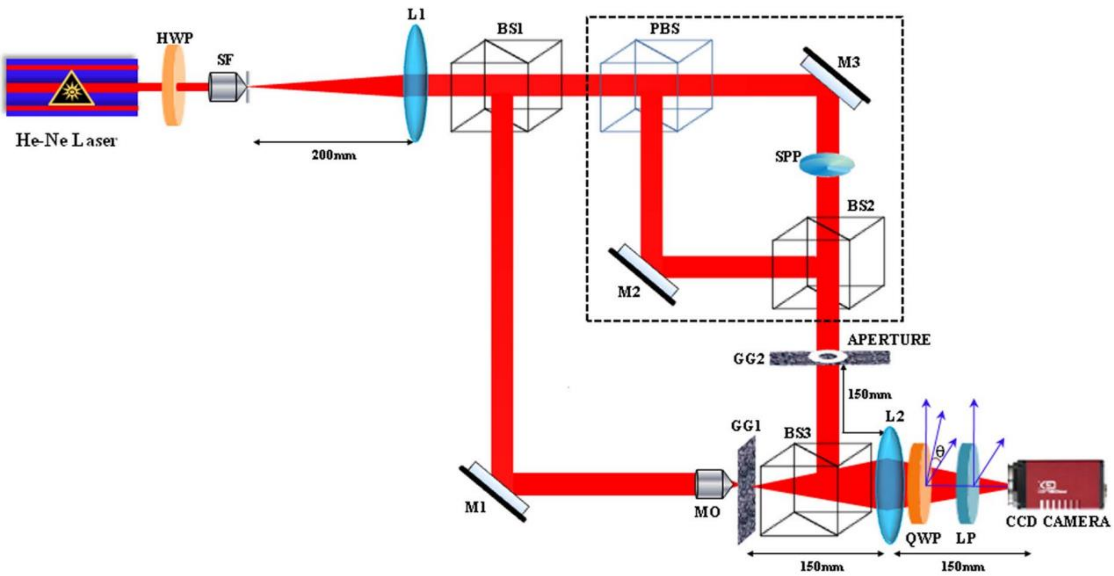

Fig. 1.23 Schematics of the experimental setup for synthesis and analysis of BCP matrix [204].

Later, Cai et al. proposed a generalized HBT experiment using fully coherent reference fields with a controllable phase difference. This enhanced method robustly measured both amplitude and phase information of the complex correlation matrix for scalar random light fields [206, 207]. Here, we have briefly discussed this generalized HBT methodology. This approach introduces two coherent reference field vectors, $U^{R1}(\boldsymbol{r})$ and $U^{R2}(\boldsymbol{r})$, each with a controllable phase delay. These reference fields are combined with the realization of the partially coherent vector light to form two composite fields, expressed as

$$U^{C1}(\boldsymbol{r}) = U^{R1}(\boldsymbol{r}) + U(\boldsymbol{r}), \tag{1.78}$$

$$U^{C2}(\boldsymbol{r}) = U^{R2}(\boldsymbol{r}) + U(\boldsymbol{r}), \tag{1.79}$$

where $U(\boldsymbol{r}) = \left[U_x(\boldsymbol{r})U_y(\boldsymbol{r})\right]^T$ is the field realization consists of two components, $U_x(\boldsymbol{r})$ and $U_y(\boldsymbol{r})$, which represent the vector field's magnitudes along the mutually perpendicular *x*- and *y*-axes.

The intensity-intensity cross-correlation of the two composite fields is given by

$$G^C_{\alpha\beta}(\boldsymbol{r}_1, \boldsymbol{r}_2) = \langle I^{C1}_\alpha(\boldsymbol{r}_1) I^{C2}_\beta(\boldsymbol{r}_2)\rangle, \tag{1.80}$$

where $I^{C1}_\alpha(\boldsymbol{r}_1)$ and $I^{C1}_\beta(\boldsymbol{r}_2)$ are the random intensities of the α and β components of the first and second composite fields, respectively.

By substituting the composite field equations and using the Gaussian moment theorem, the correlation becomes

$$G^C_{\alpha\beta}(\boldsymbol{r}_1, \boldsymbol{r}_2) = \langle I^{U1}_\alpha(\boldsymbol{r}_1)\rangle\langle I^{U2}_\beta(\boldsymbol{r}_2)\rangle + \left|W_{\alpha\beta}(\boldsymbol{r}_1, \boldsymbol{r}_2)\right|^2 +$$

$$2\sqrt{I^{R1}_\alpha(\boldsymbol{r}_1) I^{R2}_\beta(\boldsymbol{r}_2)}\, Re\left[e^{i\Delta\phi_{\alpha\beta}} W_{\alpha\beta}(\boldsymbol{r}_1, \boldsymbol{r}_2)\right], \tag{1.81}$$

where,

- $I_\alpha^{U1}(\boldsymbol{r}) = I_\alpha^{R1}(\boldsymbol{r}) + I_\alpha(\boldsymbol{r})$, and similarly, for $I_\beta^{U2}(\boldsymbol{r})$,
- $W_{\alpha\beta}(\boldsymbol{r}_1, \boldsymbol{r}_2)$ represents the complex coherence matrix,
- $\Delta\phi_{\alpha\beta} = \text{Arg}[E_\alpha^{R1}(\boldsymbol{r}_1)] - \text{Arg}[E_\beta^{R2}(\boldsymbol{r}_2)]$ is the phase difference between reference components.

By adjusting the phase delay $\Delta\phi_{\alpha\beta}$ to 0 or π/2, the real or imaginary parts of $W_{\alpha\beta}(\boldsymbol{r}_1, \boldsymbol{r}_2)$ can be isolated. Consequently, both modulus and phase information of the correlation matrix are embedded in $G_{\alpha\beta}^{C}(\boldsymbol{r}_1, \boldsymbol{r}_2)$.

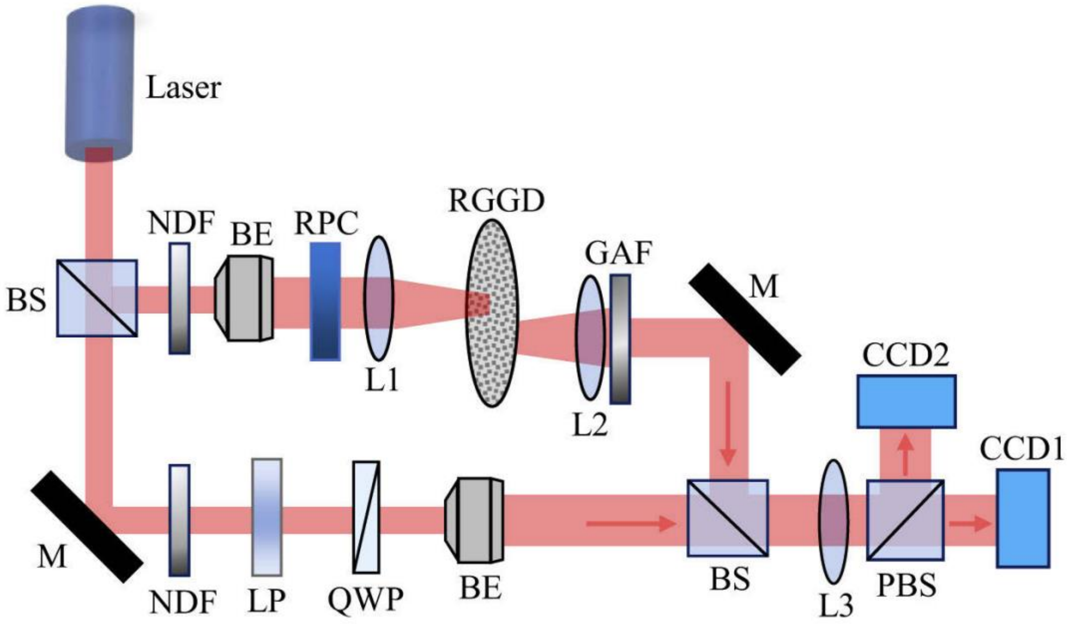

Fig. 1.24 Schematics of the experimental setup based on generalized HBT approach [206].

The experimental setup for generating the vector beam and measuring its complex correlation matrix is depicted in Fig. 1.24. The system is divided into two main components: the top arm for producing the vector beam and the bottom arm for preparing coherent reference vector fields. The intensity distributions of the *x*- and *y*-components of the reference fields, denoted as $I_x^{R1}(\boldsymbol{r})$, $I_y^{R1}(\boldsymbol{r})$, $I_x^{R2}(\boldsymbol{r})$, and $I_y^{R2}(\boldsymbol{r})$, are recorded. These reference beams are then combined with the vector beam using a beam splitter (BS). The composite beams *x*- and *y*- components are separated by a polarization beam splitter (PBS) and projected onto CCD1 and CCD2 via a $2f$ imaging system. The intensity-intensity correlations, $G^{C}_{\alpha\beta}(\boldsymbol{r}_1, \boldsymbol{r}_2, \Delta\phi_{\alpha\beta})$, are calculated using the measured intensity distributions. At a phase delay of $\Delta\phi_{\alpha\beta} = 0$, the correlation is determined as $G^{C}_{\alpha\beta}(\boldsymbol{r}_1, \boldsymbol{r}_2, \Delta\phi_{\alpha\beta} = 0) = \langle I^{C1}_{\alpha}(\boldsymbol{r}_1) I^{C2}_{\beta}(\boldsymbol{r}_2)\rangle$. For $\Delta\phi_{\alpha\beta} = \pi/2$, it becomes $G^{C}_{\alpha\beta}(\boldsymbol{r}_1, \boldsymbol{r}_2, \Delta\phi_{\alpha\beta} = \pi/2) = \langle I^{C1}_{\alpha}(\boldsymbol{r}_1) I^{C2}_{\beta}(\boldsymbol{r}_2)\rangle$. Similarly, $G^{U}_{\alpha\beta}(\boldsymbol{r}_1, \boldsymbol{r}_2) = \langle I^{U1}_{\alpha}(\boldsymbol{r}_1) I^{U2}_{\beta}(\boldsymbol{r}_2)\rangle$. These results are then used in conjunction with prior equations to reconstruct the complex correlation matrix of the vector beam, providing a complete characterization of its spatial coherence and polarization properties. These methods offer a robust framework for investigating complex coherence properties in vector fields.

1.5.7.5 Self-referencing holography

A method utilizing self-referencing holography has been reported for efficiently measuring each component of the CSD matrix for a vector beam [208]. Unlike conventional approaches, this method does not require a reference arm or prior knowledge of the light field. It effectively measures the entire 2×2 complex matrix with a two-dimensional distribution using 18 intensity patterns. In this technique shown in Fig. 1.25, after the partially coherent vector beam passes through a quarter-wave plate (QWP) and a polarizer (P), it is converted into a scalar field $W_{\theta\varepsilon}(r_1, r_2)$. The angles θ (between the QWP's fast axis and the *x*-axis) and ε (between the linear polarizer and *x*-axis) induce phase shifts between the *x*- and *y*- components of the stochastic electromagnetic beam. The scalar CSD function can then be expressed as

$$W_{\theta\varepsilon}(\boldsymbol{r}_1, \boldsymbol{r}_2) = W_{xx}(\boldsymbol{r}_1, \boldsymbol{r}_2)\cos^2\theta + W_{xy}(\boldsymbol{r}_1, \boldsymbol{r}_2) exp(-i\varepsilon)\cos\theta\sin\theta + W_{yx}(\boldsymbol{r}_1, \boldsymbol{r}_2) exp(i\varepsilon)\cos\theta\sin\theta + W_{yy}(\boldsymbol{r}_1, \boldsymbol{r}_2)\sin^2\theta, \tag{1.82}$$

The diagonal terms $W_{xx}(\boldsymbol{r}_1,\boldsymbol{r}_2)$ and $W_{yy}(\boldsymbol{r}_1,\boldsymbol{r}_2)$ are measured by aligning the polarizer parallel to x and y-axes, respectively. This ensures $\cos\theta = 1$, $\sin\theta = 0$ for $W_{xx}(\boldsymbol{r}_1,\boldsymbol{r}_2)$, and $\cos\theta = 0$, $\sin\theta = 1$ for $W_{yy}(\boldsymbol{r}_1,\boldsymbol{r}_2)$. To extract the real and imaginary parts of $W_{xy}(\boldsymbol{r}_1,\boldsymbol{r}_2)$, phase delays are introduced by controlling the QWP's fast axis and polarizer. The expressions for the components are derived as

$$\mathrm{Re}\left[W_{xy}(\boldsymbol{r}_1,\boldsymbol{r}_2)\right] = \frac{1}{2}\left[W_{\pi/4,0}(\boldsymbol{r}_1,\boldsymbol{r}_2) - W_{3\pi/4,0}(\boldsymbol{r}_1,\boldsymbol{r}_2)\right], \tag{1.83}$$

$$\mathrm{Im}\left[W_{xy}(\boldsymbol{r}_1,\boldsymbol{r}_2)\right] = \frac{1}{2i}\left[W_{3\pi/4,\pi/2}(\boldsymbol{r}_1,\boldsymbol{r}_2) - W_{\pi/4,\pi/2}(\boldsymbol{r}_1,\boldsymbol{r}_2)\right], \tag{1.84}$$

The measurement involves phase modulation at specific points, $\boldsymbol{r}_0$, introducing perturbations $\phi_1 = 0$, $\phi_2 = -2\pi/3$, and $\phi_3 = +2\pi/3$. The recorded intensity patterns I_1, I_2, and I_3 in the Fourier plane allow for reconstructing the self-referenced hologram.

Fig. 1.25 shows the experimental setup where initial part is implemented for the generation of partially coherent vector beam and later part for the measurement of CSD matrix.

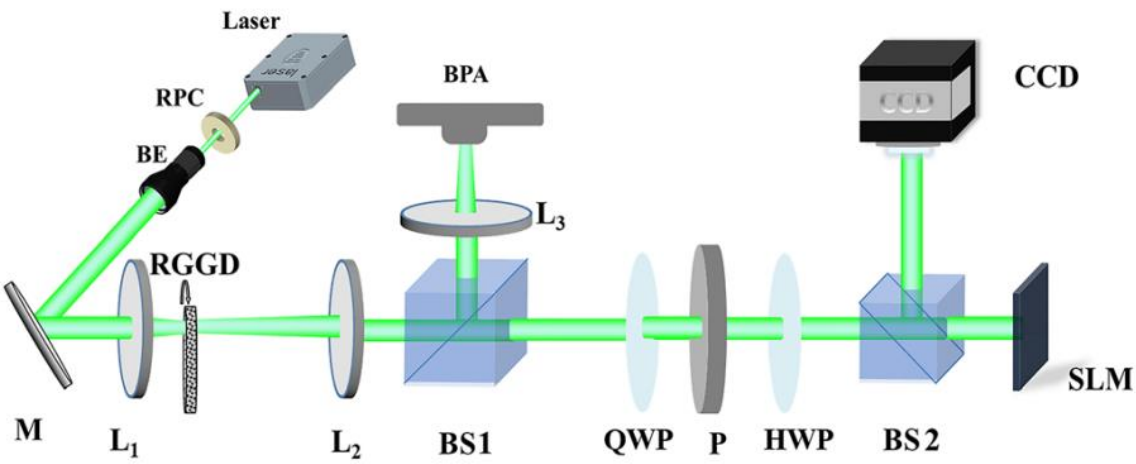

Fig. 1.25 Schematics of the experimental setup based on self-referencing holography [208].

For measurement, the experimental setup employs the second arm of BS1, which directs the beam toward a quarter-wave plate (QWP) and a polarizer. A half-wave plate (HWP) follows this configuration, aligning the polarization of the incident beam to the *x*-axis of a reflective, phase-only SLM. The SLM is positioned in the measurement plane and serves to introduce a phase perturbation at a specified point, $r_0 = 0$, within the target vector beam. In the focal plane, a CCD captures intensity patterns for various perturbation values at $r_0 = 0$. Using these recorded intensity patterns, the CSD matrix is derived. This self-referencing approach ensures robust recovery of the CSD matrix for partially coherent sources with minimal setup complexity.

Recent advancements in the measurement of vectorial coherence have introduced innovative techniques such as the utilization of nanoscatterers, which exploit nanoscale interactions to probe the coherence properties of light fields with high precision [209]. Additionally, folded interferometers have emerged as a robust tool for this purpose, offering compact designs and enhanced sensitivity for analyzing complex coherence structures [210, 211]. These developments significantly enhance the capability to study and characterize vectorial coherence in diverse optical systems.

1.6 Vortices in low coherent light

Singular optics traditionally focuses on phase singularities in monochromatic coherent fields, where the field amplitude becomes zero, creating optical vortices. Schouten et al., has expanded this concept to phase singularities in two-point coherence functions, identifying points where the spectral degree of coherence vanishes [212]. Around these points, the phase of the spectral degree of coherence forms a vortex structure, referred to as coherence vortices (CVs) or correlation singularities. Therefore, in the propagation of partially coherent vortex beams (PCVBs), the phase singularities associated with zero-intensity points gradually diminish due to random fluctuations. Nevertheless, CVs emerge in the CSD function, where the phase is undefined, preserving singularities in the two-point correlation domain. These CVs persist despite intensity averaging and represent unique correlation features that are robust against fluctuations. Theoretical predictions of CVs were first made by Gbur and Visser, who demonstrated their existence in partially coherent beams, showing their helical phase structure in the correlation domain [213, 214]. The experimental realization of CVs as ring dislocations in the cross-correlation function was later achieved by Palacios et al. [215]. Subsequent work by Wang et al. revealed the generic form of CVs, including their characteristic helical phase profiles and their connection to complex spatial coherence functions [216]. Additionally, Wang and Takeda applied these findings to establish a law of coherence conservation and explore local properties of phase singularities within spatial coherence functions [217]. CVs represent a fascinating extension of singular optics, offering insights into the interplay between coherence and spatial structure. These studies provide a foundation for understanding and manipulating light fields in advanced imaging, communication, and optical system design.

1.7 Objective of the thesis

The aforesaid sections review the current research on measuring spatial coherence in both scalar and vector domains. In the vector domain, the unification of polarization and coherence theories enables a deeper understanding of the polarization behavior of electromagnetic beams. This thesis extends the scope by introducing novel experimental methods and results for measuring vectorial coherence. The research also explores optical vortices in coherent light. With advancements in coherence theory, the focus expanded to the generation of vortices in low-coherent light, valued for its resilience in challenging environments. This thesis proposes innovative techniques for generating such vortices, addressing their unique applications and expanding their utility.

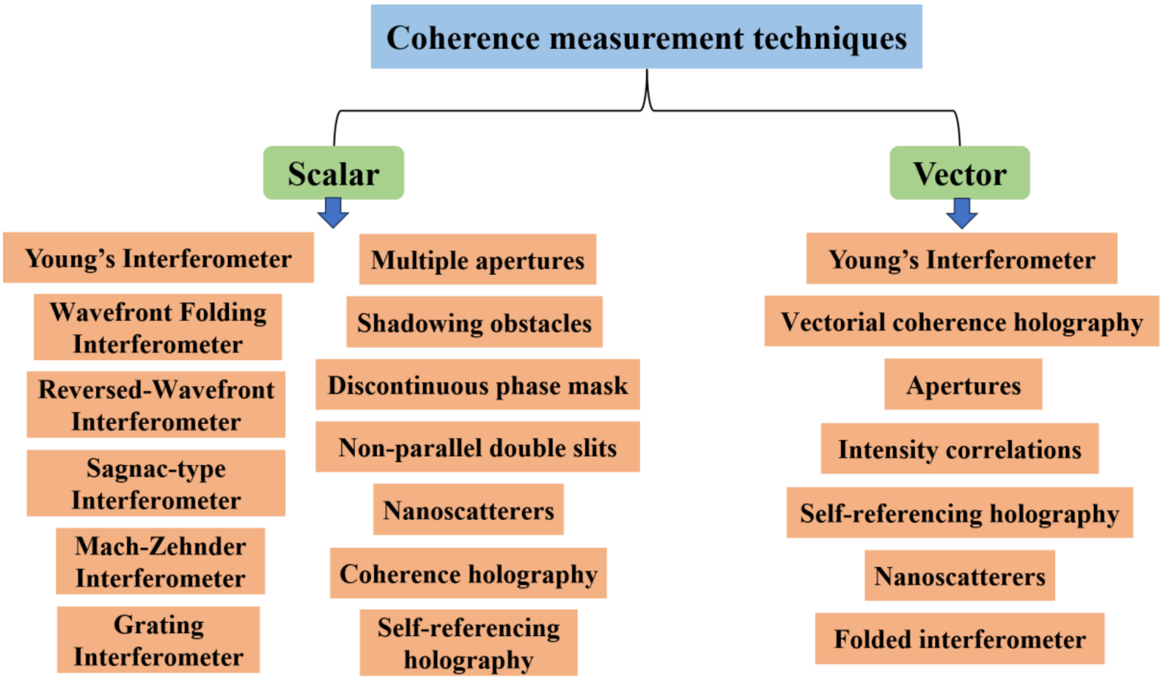

Fig. 1.26 Existing techniques for coherence measurement.